A three-dimensional unstructured mesh finite element shallow-water model, with application to the flows around an island and in a wind-driven, elongated basin*

Laurent White[1,2,†], Eric Deleersnijder[2,1], Vincent Legat[1]

April 17, 2008

[1]Université catholique de Louvain
Centre for Systems Engineering and Applied Mechanics (CESAME)
4, Avenue G. Lemaître, 1348 Louvain-la-Neuve, Belgium

[2]Université catholique de Louvain
G. Lemaître Institute of Astronomy and Geophysics (ASTR)
2, Chemin du Cyclotron, 1348 Louvain-la-Neuve, Belgium

Abstract

We present a new three-dimensional, unstructured mesh finite element shallow-water model. The current configuration is suitable for studying unstratified flows and the evolution of passive tracers. The model has a free surface and is hydrostatic. The mesh is unstructured in the horizontal and extruded towards the seabed in the direction parallel to the local gravity vector to generate a mesh made up of prisms. The mesh moves in the vertical and accommodates the free-surface motions. We describe the numerical treatment of the hydrodynamical equations with the finite element method. A discontinuous representation is used in the vertical for all velocity components. The horizontal velocity components are non-conforming in the horizontal, which is particularly appropriate for advection-dominated flows. The model is validated against a realistic tidal flow around a shallow-water island for which field measurements are available and is shown to operate successfully. The three-dimensional character of the flow is emphasized by use of a passive tracer. We also assess the model's ability to represent the vertical structure of the horizontal flow field by applying it to a wind-driven flow experiment in an elongated rectangular basin.

1 Introduction

Unstructured meshes for marine modeling offer some attractive features such as the faithful representation of the domain geometry (coastlines, bathymetry, narrow straits, sills, etc.) and the possibility of enhancing the mesh resolution in regions where it is desired (Lynch et al., 1996; Legrand et al., 2000; Piggott et al., 2005; Legrand et al., 2006, 2007; Greenberg et al., 2007). The finite element method (FEM) offers a few more advantages in addition to the use of unstructured meshes. It also provides a rigorous mathematical framework and affords a great flexibility in the choice of interpolation. Despite this, the last three decades of numerical ocean modeling have been mostly dominated by finite-difference models using structured grids with the notable exception of a few applications of the FEM in coastal, shelf and estuarine areas (Lynch and Werner, 1987, 1991; Walters and Werner, 1989; Walters, 1992; Luettich and Westerink, 1995; Ballantyne et al., 1996; Lynch et al., 1996; Fortunato et al., 1997; Cushman-Roisin and Naimie, 2002; Pietrzak et al., 2005; Walters, 2005; Pietrzak et al., 2006; White and Deleersnijder, 2007) and for tidal predictions (Le Provost et al., 1995) with a success that is not disputed. The idea of using the FEM for ocean modeling together with unstructured meshes dates back to the work by Fix (1975), who allegedly was the first to recognize the potential of variable mesh resolution for ocean flows. Note that the finite volume method (e.g., Casulli and Walters, 2000; Chen et al., 2003; Ham et al., 2005; Fringer et al., 2006; Stuhne and Peltier, 2006) and the spectral element

*Revised manuscript submitted to Ocean Modelling on 07 January 2008.
†Corresponding author. Now at Princeton/GFDL, 201 Forrestal Road, Princeton, NJ 08540, USA. Email: laurentw@princeton.edu.

method (e.g., Haidvogel et al., 1997; Iskandarani et al., 2003; Levin et al., 2006) also offer the possibility of using unstructured meshes.

It is not until the second half of the nineties that more effort was put into the development of diagnostic global ocean models on unstructured meshes (e.g., Myers and Weaver, 1995; Greenberg et al., 1998). Early issues, often cited as reasons to avoid the FEM, started to be addressed in parallel. Le Roux et al. (1998) examined the properties of several low-order finite element pairs in the context of the shallow-water equations and assessed their ability to maintain a noise-free geostrophic equilibrium. The issue of spurious computational velocity and elevation modes arising with the shallow-water equations when using the same interpolant for all variables was further addressed to select the appropriate low-order mixed formulation (Hua and Thomasset, 1984; Hanert et al., 2003; Le Roux, 2005; Le Roux et al., 2005). In the past, research focused on finding a modified form of the equations that did not support spurious modes. This led to the wave equation method (Lynch and Gray, 1979), used successfully for coastal and estuarine modeling with a harmonic decomposition in time (e.g., Kinnmark, 1986; Lynch and Werner, 1987; Walters, 1992; Fortunato et al., 1997; Greenberg et al., 1998) or with a time-stepping approach (e.g., Walters and Werner, 1989; Lynch et al., 1996). The wave equation model is obtained by operating on the two-dimensional shallow-water equations to form a wave equation in terms of the free surface elevation. This method allows to use simple linear elements for the velocity and elevation and is very accurate for general wave problems but experiences accuracy and stability issues with the advection terms (Kolar et al., 1994). In addition, the wave equation form sacrifices the primitive continuity equation, which is no longer satisfied in a discrete sense. This implies continuity (or mass) imbalances (Dawson et al., 2006; Massey and Blain, 2006) and renders the method less suitable for coupling with transport equations, let alone for long time integrations (more than several years) for which conservation is crucial. For these applications involving the transport of scalar quantities, the primitive equations approach is preferable and this is the choice we make in this work.

The finite element models by Myers and Weaver (1995), Greenberg et al. (1998) and Nechaev et al. (2003) were diagnostic and it is somewhat regrettable that almost three decades have been necessary since the work by Fix (1975) until the development of prognostic, unstructured mesh, finite element global ocean models (Danilov et al., 2004; Ford et al., 2004a,b; Danilov et al., 2005; Pain et al., 2005). In addition to the early problems cited above, we may advance a few reasons for the lack of enthusiasm from the ocean modeling community in using the FEM. First, the finite difference method is computationally cheaper than the FEM. This is probably one of the main drawbacks of the latter when considering climate simulations over decades and centuries. Even though computer speed will continue to increase in the future, the finite difference method will most likely always outperform the FEM in terms of rapidity. Second, the finite difference method is easier to implement, which is essentially due to the structured character of the grid. Third, the FEM was first applied to steady-state elliptic problems, a context in which the method performed remarkably well. However, most of the ocean dynamics is advection-dominated and, therefore, does not naturally lend itself to the use of the FEM.

It is the authors' belief that the first reason – efficiency of the finite difference method – must be of primary concern when designing a finite element global ocean model (Lynch and Werner, 1991; Danilov et al., 2005; Walters, 2006). The use of unstructured meshes should not be too detrimental to the efficiency of numerical computations and, surely, some features of earlier models should be carried over to the second-generation models, such as that described in this paper. The second reason – the implementation – is a one-time effort and should not remain an obstacle if the method is deemed valuable. As for the third reason, although finding an accurate, efficient and stable advection scheme remains an outstanding issue (Walters, 2006), a few efficient techniques have been recently proposed (Hanert et al., 2004; Iskandarani et al., 2005) that pave the way toward robust methods.

This work is motivated by the aim of building the unstructured-mesh, finite element, hydrostatic, free-surface ocean model SLIM[1]. This model should be able to accommodate a wide variety of flows, such as estuarine, coastal, shelf, basin-scale and general circulation flows. A few validation steps have already been achieved in the fields of unstructured mesh generation (Legrand et al., 2000, 2007, 2006), inertia-gravity waves propagation (Hanert et al., 2003; White et al., 2006b), advection schemes (Hanert et al., 2004), nonlinear shallow-water equations (Hanert et al., 2005), turbulence closure (Hanert et al., 2006; Blaise et al., 2007) and barotropic instabilities (White et al., 2006a). All the above studies were carried out in one- or two-dimensional frameworks. A recent paper by the same authors deals with three-dimensional tracer conservation and consistency and the computation of the vertical velocity on prismatic meshes (White et al., 2007).

In this paper, we wish to present a three-dimensional finite element model built upon what has been previously

[1]Second-generation Louvain-la-Neuve Ice-ocean Model, `http://www.climate.be/SLIM`.

done. In particular, it is based on the $P_1^{NC} - P_1$ finite element pair, which, together with the RT_0 pair, is now considered one of the most effective for simulating shallow-water flows (Hanert et al., 2005; Le Roux, 2005; Le Roux et al., 2005; Walters, 2006). The current three-dimensional model is barotropic and lacks some important components that make up the multi-purpose model that we aim to build. Nonetheless, before further enhancing the model, it is indispensable to validate it in its current configuration. The objectives of this paper are therefore to describe the model and validate it against an appropriate, realistic flow. The tidal flow around Rattray Island (Great Barrier Reef, Australia) is an ideal test case for the following reasons: (i) in situ measurements of velocity and elevation are available (Wolanski et al., 1984), (ii) the island lies in well-mixed water and a barotropic model is justified, (iii) despite the lack of baroclinicity, the flow is strongly three-dimensional (Wolanski et al., 1984; Wolanski and Hamner, 1988; Deleersnijder et al., 1992), (iv) advection and bottom friction play crucial roles in the formation of stable eddies downstream of the island (Ingram and Chu, 1987; Falconer et al., 1986; Tomczak, 1988). Hence, several model features may be assessed. We also verify the model's ability to represent the vertical structure of the horizontal flow field in a wind-driven elongated basin, which is a test case inspired by Winant (2004).

In Section 2, we present the model equations. The numerical technique, including the spatial discretization and the time-stepping algorithm, is described in Section 3. The model is applied to the region of Rattray Island and validated against field data in Section 4 and applied to the wind-driven flow in an elongated basin in Section 5.

2 Mathematical formulation

Let $\Omega(t)$ be the three-dimensional, time-dependent domain of interest. It is bounded below by the seabed, defined by Γ_b and above by the free surface, defined by Γ_s (Figure 1). The seabed is considered time-independent. The free surface, on the other hand, is time-dependent. The lateral boundary, defined by Γ_n, is parallel to the z-direction and has a constant (x, y)-position. The domain boundary can be written as $\partial\Omega = \Gamma_n \cup \Gamma_b \cup \Gamma_s$, where Γ_n comprises both open and closed lateral boundaries. The unperturbed surface defined by $z = 0$ is noted $\mathcal{T}$. We work within the scope of the hydrostatic approximation and assume constant fluid density (ρ_0).

2.1 Governing equations

The three-dimensional velocity components are noted u, v and w, in the x-, y- and z-direction respectively. We also define $\mathbf{u} = (u, v)$ to be the horizontal velocity vector. The free-surface elevation (η) is defined with respect to the constant reference height $z = 0$ taken to be the mean sea level. The horizontal components of the three-dimensional momentum equation read:

$$\frac{\partial \mathbf{u}}{\partial t} + \boldsymbol{\nabla} \cdot (\mathbf{u}\mathbf{u}) + \frac{\partial}{\partial z}(w\mathbf{u}) + f\mathbf{e}_z \wedge \mathbf{u} = -g\boldsymbol{\nabla}\eta + \mathbf{D} + \frac{\partial}{\partial z}\left(\nu_z \frac{\partial \mathbf{u}}{\partial z}\right) \qquad \text{in } \Omega, \tag{1}$$

where f is the Coriolis parameter, $\mathbf{e}_z$ is the upward-pointing unit vector, g is the gravitational acceleration, ν_z is the vertical momentum diffusion coefficient and $\boldsymbol{\nabla}$ is the horizontal gradient operator. Horizontal momentum diffusion is parameterized by $\mathbf{D}$. Equation (1) is complemented with the continuity equation

$$\boldsymbol{\nabla} \cdot \mathbf{u} + \frac{\partial w}{\partial z} = 0 \qquad \text{in } \Omega, \tag{2}$$

and the free-surface elevation equation

$$\frac{\partial \eta}{\partial t} + \boldsymbol{\nabla} \cdot \left(\int_{-d}^{\eta} \mathbf{u}\, dz \right) = 0 \qquad \text{on } \mathcal{T}, \tag{3}$$

where d is the local unperturbed depth so that the total height is defined as $H(x, y, t) = d(x, y) + \eta(x, y, t)$ (Figure 1). Finally, a given passive tracer with concentration C obeys an advection-diffusion equation (with no source term) of the form

$$\frac{\partial C}{\partial t} + \boldsymbol{\nabla} \cdot (\mathbf{u}C) + \frac{\partial (wC)}{\partial z} = \boldsymbol{\nabla} \cdot (\kappa_h \boldsymbol{\nabla} C) + \frac{\partial}{\partial z}\left(\kappa_z \frac{\partial C}{\partial z}\right) \qquad \text{in } \Omega, \tag{4}$$

where κ_h and κ_z are the eddy diffusivity coefficients in the horizontal and vertical directions, respectively.

2.2 Parameterizations

The horizontal momentum diffusion term $\mathbf{D}$ and the vertical momentum diffusion term both parameterize the effect of unresolved, small-scale processes on the resolved scales (Blumberg and Mellor, 1987; Griffies and Hallberg, 2000). However, horizontal momentum diffusion is generally employed both for physical parameterization and to ensure numerical stability (Griffies and Hallberg, 2000; Griffies et al., 2000). With unstructured meshes, it is not uncommon to have the mesh size vary by up to two orders of magnitude between different parts of the domain (e.g., Foreman et al., 1995; Legrand et al., 2007, 2006). The range of unresolved scales thus varies widely within the domain of interest, which motivates the use of a non-constant viscosity coefficient (ν_h). The Smagorinsky viscosity (Smagorinsky, 1963) is a function of the local horizontal rate of deformation times the local mesh size. In our model, the following expression is used:

$$\nu_h = c_s \Delta^2 \left(\boldsymbol{\epsilon} : \boldsymbol{\epsilon}\right)^{1/2}, \tag{5}$$

where c_s is a nondimensional constant, Δ is the local mesh size and $\boldsymbol{\epsilon}$ is the two-dimensional strain-rate tensor expressed in terms of the horizontal velocity $\mathbf{u}$:

$$\boldsymbol{\epsilon} = \begin{bmatrix} \frac{\partial u}{\partial x} & \frac{1}{2}\left(\frac{\partial u}{\partial y} + \frac{\partial v}{\partial x}\right) \\ \frac{1}{2}\left(\frac{\partial v}{\partial x} + \frac{\partial u}{\partial y}\right) & \frac{\partial v}{\partial y} \end{bmatrix}. \tag{6}$$

For triangular meshes, Δ^2 is taken to be the surface area of the triangle (Akin et al., 2003). A Laplacian form is considered for the momentum friction term $\mathbf{D}$:

$$\mathbf{D} = \frac{\partial}{\partial x}\left(\nu_h \frac{\partial \mathbf{u}}{\partial x}\right) + \frac{\partial}{\partial y}\left(\nu_h \frac{\partial \mathbf{u}}{\partial y}\right). \tag{7}$$

The Smagorinsky scheme enhances momentum diffusion in regions of large horizontal shear while reducing it in regions of smaller mesh spacing.

Similar to Fischer et al. (1979) and Deleersnijder et al. (1992), for unstratified shallow seas, the vertical momentum diffusion coefficient is defined as

$$\nu_z = \kappa u_* \left(d + z\right)\left(1 - 0.6\frac{d+z}{H}\right), \tag{8}$$

where κ is the von Karman constant and u_* is the bottom friction velocity, which obeys the following equality

$$u_*^2 = \frac{\|\boldsymbol{\tau}^b\|}{\rho_o}. \tag{9}$$

In the right-hand side of (9), $\|\cdot\|$ is the Euclidian norm and $\boldsymbol{\tau}^b$ denotes the bottom stress. The latter is parameterized by the following logarithmic law:

$$\boldsymbol{\tau}^b(x, y, \xi_b)/\rho_0 = \left[\frac{\kappa}{\ln(\xi_b/\xi_0)}\right]^2 \|\mathbf{u}_b(x, y, \xi_b)\|\mathbf{u}_b(x, y, \xi_b), \tag{10}$$

in which ξ_b is the distance to the seabed where the appropriate bottom velocity $\mathbf{u}_b$ is defined and ξ_0 is the roughness length. It should be pointed out that this turbulence closure remains very simple. It was however designed for unstratified, shallow seas (Fischer et al., 1979) and it thus appropriate for modeling the flow around Rattray island.

2.3 Boundary conditions

The lateral boundary Γ_n is deemed closed in the following discussion. The horizontal velocity $\mathbf{u}$ is subject to a condition of no-normal flow and full slip on the lateral boundary Γ_n:

$$\mathbf{u} \cdot \mathbf{n} = 0 \quad \text{and} \quad \nu_h \frac{\partial u_t}{\partial n} = 0 \quad \text{on} \quad \Gamma_n, \tag{11}$$

where u_t is the velocity component tangential to Γ_n and $\frac{\partial}{\partial n}$ is the normal derivative operator, defined as

$$\frac{\partial}{\partial n} = \frac{\partial}{\partial x} n_x + \frac{\partial}{\partial y} n_y, \tag{12}$$

with n_x and n_y the x and y components, respectively, of the three-dimensional outward-pointing unit normal to $\partial\Omega$. Note that we could also assume partial slip on the lateral boundaries, amounting to a loss of momentum through lateral stress. At the bottom, a slip condition is enforced on the horizontal velocity by relating the bottom momentum flux to the bottom velocity:

$$\nu_z \frac{\partial \mathbf{u}}{\partial z} = \frac{\boldsymbol{\tau}^b}{\rho_0} \quad \text{on } \Gamma_b, \tag{13}$$

where $\boldsymbol{\tau}^b/\rho_0$ is given by (10). At the free surface, the wind stress may be taken into account:

$$\nu_z \frac{\partial \mathbf{u}}{\partial z} = \frac{\boldsymbol{\tau}^s}{\rho_0} \quad \text{on } \Gamma_s, \tag{14}$$

where $\boldsymbol{\tau}^s$ is the surface wind stress. The usual kinematic boundary conditions are presribed:

$$\mathbf{u} \cdot \mathbf{n} + w n_z = 0 \qquad \text{on } \Gamma_b, \tag{15}$$

$$\mathbf{u} \cdot \mathbf{n} + w n_z = \frac{\partial \eta}{\partial t} n_z \qquad \text{on } \Gamma_s, \tag{16}$$

where n_z is the z component of the outward-pointing unit normal to $\partial\Omega$. The open boundary conditions depend on the problem at hand and usually involve prescribing the normal velocity and/or a linear combination of the normal velocity and the elevation such as a radiation condition. For simplicity, we do not deal with open boundary conditions in the numerical treatment of the equations and refer the reader to the work by Blayo and Debreu (2005). Finally, a condition of no diffusive flux is prescribed at the boundary for the tracer:

$$\kappa_h \frac{\partial C}{\partial n} + \kappa_z \frac{\partial C}{\partial z} n_z = 0 \qquad \text{on } \partial\Omega. \tag{17}$$

3 Numerical procedure

In this section, we describe the numerical technique used to solve the equations presented above. We do not, however, present the discretization of the tracer equation. This is done in detail by White et al. (2007) with the issues of consistency and conservation in mind. To the authors' knowledge, the finite element discretization presented in this paper is novel by its use of the three-dimensional prismatic, non-conforming element for marine modeling. In particular, the method departs markedly from that presented by Lynch and Werner (1991) and Walters (1992) in the way velocity nodes are spatially positioned. Moreover, our model is not based upon the wave equation derived by Lynch and Gray (1979) and subsequently employed in applications by e.g., Lynch and Werner (1987), Walters (1992) and Foreman et al. (1995), but relies instead on a time-stepping algorithm, the latter being better-suited for advection-dominated flows (Walters, 2005).

3.1 Mesh Topology

The numerical solution is sought in the three-dimensional domain Ω^h. The latter consists of an approximation of the physical domain, obtained by interpolating the boundaries of topographical features and the bathymetry. Within this framework, all boundaries are also interpolated so that we have $\partial\Omega \simeq \partial\Omega^h = \Gamma_b^h \cup \Gamma_s^h \cup \Gamma_n^h$. A piecewise linear interpolation is chosen for its cost-effectiveness: it is cheap and second-order accurate.

At this point, we would like to distinguish between Γ_s^h and $\mathcal{T}^h$. While the former represents the time-dependent upper boundary of the domain, the latter is simply defined as the two-dimensional surface lying at $z = 0$ and can be understood as the upper boundary of an otherwise rigid-lid model. The three-dimensional finite element mesh is obtained by first partitioning $\mathcal{T}^h$ into N_t open non-overlapping linear triangles $\mathcal{T}_e$. That is, we have

$$\overline{\mathcal{T}^h} = \bigcup_{e=1}^{N_t} \overline{\mathcal{T}_e} \qquad \text{and} \qquad \mathcal{T}_e \cap \mathcal{T}_f = \emptyset \quad (e \neq f),$$

where $\overline{\mathcal{T}_e}$ denotes the closure of $\mathcal{T}_e$. Extrusion of each triangle $\mathcal{T}_e$ into linear prismatic columns is then performed so as to exactly fit the sea bottom Γ_b^h and the free surface Γ_s^h. In so doing, the domain Ω^h is naturally partitioned into N_p

open non-overlapping linear prisms Ω_e:

$$\overline{\Omega^h} = \bigcup_{e=1}^{N_p} \overline{\Omega_e} \qquad \text{and} \qquad \Omega_e \cap \Omega_f = \emptyset \quad (e \neq f).$$

In two dimensions, we also consider the set E^h of all inter-element edges $E_e = \partial\overline{\mathcal{T}_e} \cap \partial\overline{\mathcal{T}_f}$ with $e > f$ (Figure 2). This set comprises all edges shared between adjacent triangles belonging to $\mathcal{T}^h$. We thus have

$$\overline{E^h} = \bigcup_{e=1}^{N_e} \overline{E_e} \qquad \text{and} \qquad E_e \cap E_f = \emptyset \quad (e \neq f),$$

where N_e is the number of such inter-element edges. To each edge E_e corresponds a unique normal vector $(\mathbf{n}^e, n_z^e)$ pointing from $\mathcal{T}_e$ to $\mathcal{T}_f$. Similarly to the velocity, the horizontal components of the unit normal are written in vector form and denoted by $\mathbf{n}^e$. In three dimensions, we consider the set F^h of all inter-element vertical rectangular faces $F_e = \partial\overline{\Omega_e} \cap \partial\overline{\Omega_f}$ with $e > f$ (Figure 2). This set comprises all faces shared between adjacent prisms in adjacent columns but does not comprise those faces shared by two prisms within the same column. It is important to keep in mind that those faces remain vertical at all time. We have

$$\overline{F^h} = \bigcup_{e=1}^{N_f} \overline{F_e} \qquad \text{and} \qquad F_e \cap F_f = \emptyset \quad (e \neq f),$$

where N_f is the number of such vertical inter-element boundaries. To each face F_e corresponds a unique normal vector $(\mathbf{n}^e, n_z^e)$ pointing from Ω_e to Ω_f. Finally, the set S^h comprises those triangular faces shared by prisms within the same column, that is shared by prisms stacked upon one another. Each of those triangular faces will be noted $S_e = \partial\overline{\Omega_e} \cap \partial\overline{\Omega_f}$ with $e > f$ (Figure 2). We have

$$\overline{S^h} = \bigcup_{e=1}^{N_s} \overline{S_e} \qquad \text{and} \qquad S_e \cap S_f = \emptyset \quad (e \neq f),$$

where N_s is the number of such triangular faces. A unique normal $(\mathbf{n}^e, n_z^e)$, pointing from Ω_e to Ω_f, is associated to each triangular face S_e.

The two-dimensional mesh, that is the partition of $\mathcal{T}^h$, may be unstructured and several criteria may be selected in order to control the mesh resolution. Common refining methods are generally based on the bathymetry (see e.g., Bilgili et al., 2006). Bathymetry-based criteria may be further refined to take into account the proximity of the coast, islands and reefs (Legrand et al., 2006) or by using anisotropic elements along the shelf break (Legrand et al., 2007).

There is no a priori constraint on the location of vertical nodes but we currently require that two adjacent columns comprise the same number of prisms. Hence, the three-dimensional mesh contains the same number of layers throughout. This constraint could be relaxed in the future by allowing adjacent columns to contain different number of prisms, the transition being assured by collapsing nodes in the vertical to generate pyramids or tetrahedra. All nodes are free to move in the vertical, which allows for tracking the free surface and preventing the occurrence of overly thin layers near the surface by vertical redistribution of the nodes (Adcroft and Campin, 2004). By permitting such freedom in the mesh motion, we implicitly allow for the use of generalized vertical coordinate systems (e.g., Kasahara, 1974; Deleersnijder and Ruddick, 1989; Gerdes, 1993; Adcroft and Hallberg, 2006; Song and Hou, 2006). The mesh movement falls into the so-called Arbitrary Lagrangian-Eulerian (ALE) framework since the nodes are neither fixed in space nor do they follow the fluid.

3.2 Finite element spatial discretization

The variational statements will be written in a way that allows the use of a discontinuous representation of the horizontal velocity field in all directions whereas the elevation is taken to be continuous across elements. The variational statements involve integration over mesh geometrical items in one, two and three dimensions. The following notations

are used:

$$\int f\, d\Omega \quad : \quad \text{3D integration over prisms,}$$

$$\int f\, d\Gamma \quad : \quad \text{2D integration over vertical faces,}$$

$$\int f\, d\tau \quad : \quad \text{2D integration over triangles,}$$

$$\int f\, ds \quad : \quad \text{1D integration over edges.}$$

3.2.1 Momentum equation

For the momentum equation, the variational statement is obtained by multiplying Eq. (1) by a test function, supplementing it with appropriate discontinuity-penalization and upwinding terms (see e.g., Houston et al., 2002; Hanert et al., 2004) and integrating the result by parts over the whole domain. The variational statement consists in finding $\mathbf{u}(x,y,z,t) \in \mathcal{U} \times \mathcal{U}$ such that

$$\begin{aligned}
&\sum_{e=1}^{N_p} \frac{\mathrm{d}}{\mathrm{d}t} \int_{\Omega_e(t)} \mathbf{u}\cdot\hat{\mathbf{u}}\,\mathrm{d}\Omega + \sum_{e=1}^{N_p} \int_{\Omega_e(t)} \left[-\mathbf{u}\cdot(\mathbf{u}\cdot\boldsymbol{\nabla}\hat{\mathbf{u}}) - \tilde{w}\mathbf{u}\cdot\frac{\partial\hat{\mathbf{u}}}{\partial z} \right. \\
&\left. +(f\hat{\mathbf{e}}_z \wedge \mathbf{u})\cdot\hat{\mathbf{u}} + g\boldsymbol{\nabla}\eta\cdot\hat{\mathbf{u}} + \nu_h\frac{\partial\mathbf{u}}{\partial x}\cdot\frac{\partial\hat{\mathbf{u}}}{\partial x} + \nu_h\frac{\partial\mathbf{u}}{\partial y}\cdot\frac{\partial\hat{\mathbf{u}}}{\partial y} + \nu_z\frac{\partial\mathbf{u}}{\partial z}\cdot\frac{\partial\hat{\mathbf{u}}}{\partial z} \right] \mathrm{d}\Omega \\
&\underbrace{- \int_{\Gamma_s^h\cup\Gamma_b^h} \hat{\mathbf{u}}\cdot\left(\nu_h\frac{\partial\mathbf{u}}{\partial n} + \nu_z\frac{\partial\mathbf{u}}{\partial z}n_z\right)\mathrm{d}\tau}_{1} + \underbrace{\int_{\Gamma_s^h\cup\Gamma_b^h} (\mathbf{u}\cdot\mathbf{n} + \tilde{w}n_z)\mathbf{u}\cdot\hat{\mathbf{u}}\,\mathrm{d}\tau}_{2} \\
&\underbrace{+ \int_{\Gamma_n^h} \left[(\mathbf{u}\cdot\mathbf{n})\mathbf{u} - \nu_h\frac{\partial\mathbf{u}}{\partial n}\right]\cdot\hat{\mathbf{u}}\,\mathrm{d}\Gamma}_{3} + \underbrace{\sum_{e=1}^{N_f}\int_{F_e} <\mathbf{u}\cdot\mathbf{n}^e><\mathbf{u}>_\lambda\cdot[\hat{\mathbf{u}}]\,\mathrm{d}\Gamma}_{4} \\
&\underbrace{+ \sum_{e=1}^{N_s}\int_{S_e} <\mathbf{u}\cdot\mathbf{n}^e + \tilde{w}n_z^e><\mathbf{u}>_\lambda\cdot[\hat{\mathbf{u}}]\,\mathrm{d}\tau}_{5} - \underbrace{\sum_{e=1}^{N_s}\int_{S_e}\left\langle \nu_h\frac{\partial\mathbf{u}}{\partial n} + \nu_z\frac{\partial\mathbf{u}}{\partial z}n_z^e\right\rangle\cdot[\hat{\mathbf{u}}]\,\mathrm{d}\tau}_{6} \\
&\underbrace{+ \sum_{e=1}^{N_s}\int_{S_e}\sigma[\mathbf{u}]\cdot[\hat{\mathbf{u}}]\,\mathrm{d}\tau = 0}_{7} \quad \forall\hat{\mathbf{u}}\in\mathcal{U}\times\mathcal{U},
\end{aligned} \tag{18}$$

where $\mathcal{U}\times\mathcal{U}$ is the suitable infinite-dimensional Sobolev space such that $\mathcal{U} = \mathcal{H}^1(\Omega^h)$. A definition of this functional space is given in Appendix A. The test function $\hat{\mathbf{u}}$ belongs to $\mathcal{U}\times\mathcal{U}$ and is sufficiently well behaved that the integrals in (18) make sense.

The volume integrals occuring in Eq. (18) are computed on the three-dimensional time-dependent domain Ω^h. Since the mesh is allowed to move along the vertical axis, the nodal values of the vertical velocity w must be modified to take into account the motion of the mesh (Formaggia and Nobile, 2004). This is so because integration of advection terms is usually performed on a unique mesh at a given time step. However, the time-discretized temporal derivative of $\mathbf{u}$ is computed on two different meshes. The modification of the discrete vertical velocity accounts for the mesh motion between those two time levels. The modified vertical velocity is noted $\tilde{w} = w - w_m$, where w_m is the mesh velocity.

The seven underbraced integrals (labeled 1 to 7) arise after integration by parts of either the advection or diffusion terms. These terms are explained hereafter.

1. The first integral is an expression of the diffusive momentum flux through the sea bottom and sea surface. Use can be made of boundary conditions (13)-(14) to compute the integral.

2. The second integral expresses the advective momentum flux through the sea bottom and sea surface. The modified vertical velocity $\tilde{w}$ takes on the form (White et al., 2007)

$$\tilde{w} = \begin{cases} w & \text{on } \Gamma_b^h, \\ w - \frac{\partial \eta}{\partial t} & \text{on } \Gamma_s^h, \end{cases}$$

so that, by using boundary conditions (15) and (16), this integral is discarded. This expresses the impermeability of the seabed and sea surface.

3. The third integral is the momentum flux through the closed lateral boundary. This term may be simplified with the enforcement of boundary condition (11). The advective flux vanishes due to the no-normal flow condition. The diffusive flux is to be expressed in terms of the normal and tangential components, by noting that

$$\frac{\partial \mathbf{u}}{\partial n} = \frac{\partial u_n}{\partial n}\hat{\mathbf{n}} + \frac{\partial u_t}{\partial n}\hat{\mathbf{t}}$$

where $\hat{\mathbf{n}}$ and $\hat{\mathbf{t}}$ are the unit vectors normal and tangential, respectively, to Γ_n^h. Similarly, the vector test function $\hat{\mathbf{u}}$ can be written in terms of the normal and tangential components:

$$\hat{\mathbf{u}} = \hat{u}_n\hat{\mathbf{n}} + \hat{u}_t\hat{\mathbf{t}}.$$

4. The terms labeled 4 and 5 arise by assembling all contributions of inter-element boundary integrals from advection terms. Each one of the N_f integrals is an expression of the momentum flux by advection through the vertical face shared by two adjacent prisms. Similarly, each one of the N_s integrals is the advective flux through triangular faces shared by prisms stacked upon each other. Using the same notations as Hanert et al. (2004), we note $< f >$ the mean value of f on any face shared by two adjacent prisms and $< f >_\lambda$, its weighted average. That is,

$$< f >= \frac{1}{2} f_{|\Omega_e} + \frac{1}{2} f_{|\Omega_f}, < f >_\lambda = \left(\frac{1}{2} + \lambda\right) f_{|\Omega_e} + \left(\frac{1}{2} - \lambda\right) f_{|\Omega_f}, \tag{19}$$

for all three-dimensional elements Ω_e and Ω_f sharing a common face. The jump across the latter is noted $[f]$ and is defined by

$$[f] = f_{|\Omega_e} - f_{|\Omega_f},$$

with $f_{|\Omega_e}$ being the restriction of f on Ω_e. Note that the quantity being advected is $< \mathbf{u} >_\lambda$. In expression (19), the adjustable parameter $\lambda \in [-1/2, 1/2]$ allows for giving more weight to the local or neighboring value. In particular, taking $\lambda = \frac{1}{2}\text{sign}(\mathbf{u} \cdot \mathbf{n})$ is equivalent to an upwind-biased flux. This advection scheme was shown by Hanert et al. (2004) to be particularly effective in two dimensions. In this paper, we generalize it in three dimensions.

5. The terms labeled 6 and 7 (involving integrals over triangular faces shared by stacked prisms) originate from the integration by parts of the momentum diffusion term. Hanert et al. (2004) showed that the non-conforming nature of the interpolation in the horizontal ensures that no boundary term need be computed across vertical faces as far as momentum diffusion is concerned. The sixth sum involves integrals of centered diffusive fluxes. There is no preferred orientation associated to it. The seventh term is a weak continuity constraint and involves the discontinuity-penalization parameter σ while solving elliptic problems (Houston et al., 2002). The expression for σ is proportional to the diffusivity coefficients.

To summarize, by using the boundary conditions (13) and (14) to compute integral 1, discarding integral 2 and

simplifying integral 3, the variational statement for the momentum equation reduces to

$$
\begin{aligned}
&\sum_{e=1}^{N_p} \frac{\mathrm{d}}{\mathrm{d}t} \int_{\Omega_e(t)} \mathbf{u}\cdot\hat{\mathbf{u}}\,\mathrm{d}\Omega + \sum_{e=1}^{N_p} \int_{\Omega_e(t)} \Big[-\mathbf{u}\cdot(\mathbf{u}\cdot\boldsymbol{\nabla}\hat{\mathbf{u}}) - \tilde{w}\mathbf{u}\cdot\frac{\partial\hat{\mathbf{u}}}{\partial z} \\
&+(f\hat{\mathbf{e}}_z\wedge\mathbf{u})\cdot\hat{\mathbf{u}} + g\boldsymbol{\nabla}\eta\cdot\hat{\mathbf{u}} + \nu_h\frac{\partial\mathbf{u}}{\partial x}\cdot\frac{\partial\hat{\mathbf{u}}}{\partial x} + \nu_h\frac{\partial\mathbf{u}}{\partial y}\cdot\frac{\partial\hat{\mathbf{u}}}{\partial y} + \nu_z\frac{\partial\mathbf{u}}{\partial z}\cdot\frac{\partial\hat{\mathbf{u}}}{\partial z}\Big]\,\mathrm{d}\Omega \\
&-\int_{\Gamma_s^h}\hat{\mathbf{u}}\cdot\frac{\boldsymbol{\tau}^s}{\rho_0}n_z\,\mathrm{d}\tau - \int_{\Gamma_b^h}\hat{\mathbf{u}}\cdot\frac{\boldsymbol{\tau}^b}{\rho_0}n_z\,\mathrm{d}\tau - \int_{\Gamma_s^h\cup\Gamma_b^h}\nu_h\frac{\partial\mathbf{u}}{\partial n}\cdot\hat{\mathbf{u}}\,\mathrm{d}\tau \\
&+\sum_{e=1}^{N_f}\int_{F_e} <\mathbf{u}\cdot\mathbf{n}^e><\mathbf{u}>_\lambda\cdot[\hat{\mathbf{u}}]\,\mathrm{d}\Gamma + \sum_{e=1}^{N_s}\int_{S_e} <\mathbf{u}\cdot\mathbf{n}^e + wn_z^e><\mathbf{u}>_\lambda\cdot[\hat{\mathbf{u}}]\,\mathrm{d}\tau \\
&-\sum_{e=1}^{N_s}\int_{S_e}\left\langle \nu_h\frac{\partial\mathbf{u}}{\partial n} + \nu_z\frac{\partial\mathbf{u}}{\partial z}n_z^e\right\rangle\cdot[\hat{\mathbf{u}}]\,\mathrm{d}\tau + \sum_{e=1}^{N_s}\int_{S_e}\sigma[\mathbf{u}]\cdot[\hat{\mathbf{u}}]\,\mathrm{d}\tau = 0 \quad \forall\hat{\mathbf{u}}\in\mathcal{U}\times\mathcal{U}.
\end{aligned}
\tag{20}
$$

In the statement above, the surface integral on Γ_s^h (Γ_b^h) is positive (negative) because n_z is positive (negative) there. This respectively corresponds to a positive influx of momentum due to wind stress and a negative influx due to bottom stress. It is noteworthy that in Eq. (18), boundary integrals 5 to 7 are the only means by which information is conveyed in the vertical between elements. In other words, they arise because the horizontal velocity is discontinuous in the vertical and would disappear for a continuous interpolation.

3.2.2 Free-surface equation

For the free-surface equation, the variational statement is obtained by multiplying Eq. (3) by a test function, supplementing it with appropriate discontinuity-penalization terms and integrating the result by parts over the whole domain. The variational statement consists in finding $\eta(x,y,t)\in\mathcal{H}$ such that

$$
\int_{\mathcal{T}^h}\frac{\partial\eta}{\partial t}\hat{\eta}\,d\tau - \int_{\Omega^h}\mathbf{u}\cdot\boldsymbol{\nabla}\hat{\eta}\,d\Omega = 0 \quad \forall\hat{\eta}\in\mathcal{H}. \tag{21}
$$

where $\mathcal{H}$ is the functional space $\mathcal{L}^2(\mathcal{T}^h)$. Refer to Appendix A for a definition. The test function $\hat{\eta}$ belongs to $\mathcal{H}$.

3.2.3 Continuity equation

The continuity equation (2) is used to diagnostically compute the vertical velocity. Tracer conservation and consistency critically depend on the way the vertical velocity is computed. This aspect of the model is covered in full detail by White et al. (2007). We choose a discontinuous representation in the vertical, which implies using a discontinuous representation for tracers to ensure consistency. This is an attractive feature given the stratified nature of the ocean interior. To be consistent with the elevation, the representation is continuous is the horizontal. The variational statement is obtained by multiplying Eq. (2) by a test function, supplementing it with appropriate discontinuity-penalization and upwinding terms in the vertical and integrating the result over the whole domain. The variational statement consists in finding $w\in\mathcal{W}$ such that

$$
\begin{aligned}
&-\sum_{e=1}^{N_p}\int_{\Omega_e}\left[\mathbf{u}\cdot\boldsymbol{\nabla}\hat{w} + w\frac{\partial\hat{w}}{\partial z}\right]d\Omega + \underbrace{\sum_{e=1}^{N_s}\int_{S_e}\left(<\mathbf{u}\cdot\mathbf{n}^e> + w_{\mathtt{down}}n_z^e\right)[\hat{w}]\,d\tau}_{1} \\
&+\underbrace{\int_{\Gamma_s^h}(\mathbf{u}\cdot\mathbf{n}+wn_z)\,\hat{w}\,d\tau}_{2} + \underbrace{\int_{\Gamma_b^h}(\mathbf{u}\cdot\mathbf{n}+wn_z)\,\hat{w}\,d\tau}_{3} = 0 \quad \forall\hat{w}\in\mathcal{W}.
\end{aligned}
\tag{22}
$$

where $[\hat{w}]$ is the jump in the test function that belongs to $\mathcal{W}$, which, again, is a carefully chosen functional space to ensure that all integrals above remain finite. When computing integrals of sum 1 over interior triangular faces, the mean horizontal velocity is used whereas the vertical velocity within the lower prism is always used. This merely

amounts to integrating the continuity equation from the bottom upwards will full upwind weighting on the vertical velocity belonging to the element below the triangular face. Intuitively, the continuity equation can be viewed as a steady-state advection equation (with the advective velocity equal to one) with source term (the horizontal velocity divergence), which helps justify the approach described herebefore.

The integral over Γ_s^h (labeled 2 in Eq. 22) must be computed (it is not zero) and will provide the vertical velocity at the surface. By computing the vertical velocity in the way outlined by Eq. (22), the surface kinematic boundary condition (16) is weakly – and automatically – satisfied, consistently ensuring global tracer conservation (White et al., 2007). The last integral (labeled 3) vanishes because the sea bottom is impermeable to the flow. This is a weak enforcement of boundary condition (15). Discarding the last term of Eq. (22), we wind up with

$$\begin{aligned} &- \sum_{e=1}^{N_p} \int_{\Omega_e} \left[\mathbf{u} \cdot \boldsymbol{\nabla} \hat{w} + w \frac{\partial \hat{w}}{\partial z} \right] \, d\Omega + \sum_{e=1}^{N_s} \int_{S_e} (< \mathbf{u} \cdot \mathbf{n}^e > + w_{\mathtt{down}} n_z^e) \, [\hat{w}] \, d\tau \\ &+ \int_{\Gamma_s^h} (\mathbf{u} \cdot \mathbf{n} + w n_z) \, \hat{w} \, d\tau = 0 \quad \forall \hat{w} \in \mathcal{W}. \end{aligned} \tag{23}$$

Note that Eq. (23) reduces to Eq. (21) when $\hat{w}$ is substituted for $\hat{\eta}$, which is required for consistency.

3.2.4 Discretization

A finite element approximation to Eqs (1)-(3) can be obtained by replacing $\mathbf{u}$, η and w by their respective approximations $\mathbf{u}^h$, η^h and w^h in the variational statements (20), (21) and (23). Those approximate fields belong to finite-dimensional subspaces $\mathcal{U}^h \times \mathcal{U}^h \subset \mathcal{U} \times \mathcal{U}$, $\mathcal{H}^h \subset \mathcal{H}$ and $\mathcal{W}^h \subset \mathcal{W}$ respectively:

$$\begin{aligned} \mathbf{u} \simeq \mathbf{u}^h &= \sum_{j=1}^{N_U} \mathbf{U}_j(t) \psi_j(x,y,z) \quad \in \mathcal{U}^h \times \mathcal{U}^h \\ \eta \simeq \eta^h &= \sum_{j=1}^{N_H} H_j(t) \phi_j(x,y) \quad \in \mathcal{H}^h \\ w \simeq w^h &= \sum_{j=1}^{N_W} W_j(t) \varphi_j(x,y,z) \quad \in \mathcal{W}^h \end{aligned}$$

where $\mathbf{U}_j$, H_j and W_j are the time-dependent nodal values and ψ_j, ϕ_j and φ_j are the associated polynomial basis functions. Finally, the nodal values can be computed by resorting to the Galerkin method, which comes down to substituting $\psi_i \hat{e}_x + \psi_i \hat{e}_y$, ϕ_i and φ_i for the test functions $\hat{\mathbf{u}}$, $\hat{\eta}$ and $\hat{w}$ in (20) for $i = 1 \ldots N_U$, in (21) for $i = 1 \ldots N_H$ and in (23) for $i = 1 \ldots N_W$, respectively.

Up to this point, nothing has been said about the interpolation that we wish to consider for the variables $\mathbf{u}^h$, w^h and η^h, besides the fact that we allow discontinuities in the velocity field. The location of velocity and elevation nodes is shown in Figure (3). The horizontal velocity is linear non-conforming in the horizontal and linear discontinuous in the vertical. The representation is thus discontinuous everywhere except along a vertical line joining the nodes. This interpolation can be viewed as a generalization in three dimensions of the so-called P_1^{NC} triangular element (Hua and Thomasset, 1984). The vertical velocity is chosen to be linear continuous in the horizontal and linear discontinuous in the vertical. The elevation is linear with the nodes located at the vertices of each triangle $\mathcal{T}_e$.

3.3 Time-stepping algorithm

In order to lighten the notations, it is preferable to carry out the time discretization of Eqs (1) and (3) rather than their space-discretized counterparts. Since the vertical velocity is computed diagnostically, we shall not treat the continuity equation (2) here. Once time discretization is performed, it is straightforward to achieve discretization in space of the semi-discrete equations by following the procedure described in the previous section.

The most fundamental choice that we make in this model regarding the time discretization is to resolve all processes with the same time step. In order to circumvent the stability constraint incurred by the propagation of inertia-gravity

waves, a semi-implicit or implicit (or any level of impliciteness in between) free-surface method is required (Dukowicz and Smith, 1994). Hence, Eqs (1) and (3) must be solved simultaneously for $(\mathbf{u}^{n+1}, \eta^{n+1})$, which leads to

$$\frac{\mathbf{u}^{n+1}-\mathbf{u}^n}{\Delta t} + \boldsymbol{\nabla}\cdot(\mathbf{u}^n\mathbf{u}^n) + \frac{\partial}{\partial z}\left(w^n\mathbf{u}^n\right) + f\hat{\mathbf{e}}_z \wedge \mathbf{u}^{n+\theta} + g\boldsymbol{\nabla}\eta^{n+\theta} - \mathbf{D}^n - \frac{\partial}{\partial z}\left(\nu_z^n \frac{\partial \mathbf{u}^{n+1}}{\partial z}\right) = 0, \tag{24}$$

for the momentum equation and

$$\frac{\eta^{n+1}-\eta^n}{\Delta t} + (1-\theta)\boldsymbol{\nabla}\cdot\int_{-d}^{\eta^n}\mathbf{u}^n\,\mathrm{d}z + \theta\boldsymbol{\nabla}\cdot\int_{-d}^{\eta^{n+1}}\mathbf{u}^{n+1}\,\mathrm{d}z = 0, \tag{25}$$

for the free-surface equation. In (24) and (25), Δt is the time step and

$$g^{n+\theta} = \theta g^{n+1} + (1-\theta)g^n,$$

where $0.5 \leq \theta \leq 1.0$. The choice $\theta = 0.5$ yields a semi-implicit scheme while $\theta = 1$ leads to an implicit scheme. Unless otherwise stated, we consider a Crank-Nicolson (CN) scheme ($\theta = 0.5$). In Eq. (24), the advection and horizontal diffusion terms are explicit in time while the vertical diffusion term is implicit (with the vertical eddy viscosity coefficient taken at the previous time step). The second integral in Eq. (25) can be split into an integral over the depth at time step n and an integral over the change in depth. Neglecting the latter, we simply obtain

$$\frac{\eta^{n+1}-\eta^n}{\Delta t} + (1-\theta)\boldsymbol{\nabla}\cdot\int_{-d}^{\eta^n}\mathbf{u}^n\,\mathrm{d}z + \theta\boldsymbol{\nabla}\cdot\int_{-d}^{\eta^n}\mathbf{u}^{n+1}\,\mathrm{d}z = 0. \tag{26}$$

The solution $(\mathbf{u}^{n+1}, \eta^{n+1})$ can be found by solving the coupled system (24)-(26) involving the nodal values $(\mathbf{U}^{n+1}, H^{n+1})$. For large-scale applications, the computational overhead incurred by the resolution of this system becomes quickly unbearable. This is even more so considering the mesh is moving and the left-hand matrix of the system must be recomputed at each time step. A huge gain in performance may be obtained by splitting the dynamics into a two-dimensional depth-averaged system for the evolution of the inertia-gravity waves and a three-dimensional system for the vertical structure of the velocity (e.g., Simons, 1974; Blumberg and Mellor, 1987; Killworth et al., 1991). Those systems are sometimes called external and internal modes, respectively.

The external mode equations are the traditional shallow-water equations, obtained by integrating the momentum equation (1) over depth and coupling the result with the free-surface equation (3) written in terms of the depth-averaged velocity $\overline{\mathbf{u}}$:

$$\frac{\partial \overline{\mathbf{u}}}{\partial t} + f\hat{\mathbf{e}}_z \wedge \overline{\mathbf{u}} + g\boldsymbol{\nabla}\eta = \mathbf{B}, \tag{27}$$

$$\frac{\partial \eta}{\partial t} + \boldsymbol{\nabla}\cdot(H\overline{\mathbf{u}}) = 0, \tag{28}$$

where $\mathbf{B}$ regroups the forcing and coupling terms originating from depth-integration of advection and diffusion terms (see Appendix B). It is important to note that some of these terms may be expressed in terms of the depth-averaged velocity – i.e., in terms of prognostic variables – and therefore can be time stepped with the left-hand side of (27). However, it remains unclear which terms should be time stepped and which terms should act as depth-averaged, forcing terms. It is context-dependent and, in this study, advection and horizontal diffusion are time stepped. The finite element resolution of the shallow-water equations is well documented (Le Roux et al., 1998, 2000; Hanert et al., 2003, 2005) and will not be reproduced here. We use the scheme proposed by Hanert et al. (2005). In particular, the nodal values of the depth-averaged velocity are located at the middle of the edges joining elevation nodes. So, the depth-averaged velocity is interpolated with the so-called P_1^{NC} element (Hua and Thomasset, 1984). Note that this choice is coherent with the location of nodes for the three-dimensional horizontal velocity (see Figure 3). A theta-scheme applied to Eqs (27)-(28) gives the following time discretization

$$\frac{\overline{\mathbf{u}}^{n+1}-\overline{\mathbf{u}}^n}{\Delta t} + f\hat{\mathbf{e}}_z \wedge \overline{\mathbf{u}}^{n+\theta} + g\boldsymbol{\nabla}\eta^{n+\theta} = \mathbf{B}^n, \tag{29}$$

$$\frac{\eta^{n+1}-\eta^n}{\Delta t} + \boldsymbol{\nabla}\cdot\left(H^n\overline{\mathbf{u}}^{n+\theta}\right) = 0. \tag{30}$$

It is worth noticing that, unlike Hanert et al. (2005), Eq. (30) is not time stepped with a leap-frog scheme. The latter is to be avoided due to the existence of computational modes. Those could be time-filtered at the cost of breaking down global mass conservation (Griffies, 2004), which, in our opinion, is highly undesirable.

A closer look at Eq. (30) indicates that the transport $\mathbf{M}$ (defined as the depth-integrated horizontal velocity) whose divergence causes the change in the free-surface elevation is given by

$$\mathbf{M} = H^n \left(\theta \overline{\mathbf{u}}^{n+1} + (1-\theta) \overline{\mathbf{u}}^{n} \right). \tag{31}$$

Even by taking $\theta = 0.5$, the linearization in time of the term $H\overline{\mathbf{u}}$ in Eq. (30) precludes the transport from being formally centered in time. For being so, we ought to compute the divergence of $H^{n+\theta}\overline{\mathbf{u}}^{n+\theta}$, with $\theta = 0.5$. Although this computation would yield a time-centered transport, it has two drawbacks: (i) it requires the solution of a nonlinear system and (ii) it requires to hold in memory a mesh that is centered in time in addition to the meshes at times n and $n+1$. Therefore, we are instead favorable to solving the linearized Eq. (30) for which the change in elevation is caused by a transport computed on the geometry at time step n, that is Eq. (31) with $\theta = 0.5$. This leads to a much faster algorithm at the cost of a very small loss of accuracy. This design leads to the time staggered algorithm exposed in Section 3.4.

The three-dimensional horizontal velocity (i.e., the internal mode) is determined by solving the following equation

$$\frac{\mathbf{u}^{k+1} - \mathbf{u}^k}{\Delta t} + \boldsymbol{\nabla} \cdot \left(\mathbf{u}^k \mathbf{u}^k \right) + \frac{\partial}{\partial z} \left(w^m \mathbf{u}^k \right) + f \hat{\mathbf{e}}_z \wedge \mathbf{u}^k + g \boldsymbol{\nabla} \eta^k - \mathbf{D}^k - \frac{\partial}{\partial z} \left(\nu_z^k \frac{\partial \mathbf{u}^{k+1}}{\partial z} \right) = 0. \tag{32}$$

where $k = n - 1/2$. Note that Eq. (32) is solved alternately for u and v at one time step and then v and u at the next time step to provide a stable time stepping of the Coriolis term. The transport computed from the three-dimensional horizontal velocity field is not equal to the transport given by Eq. (31):

$$\int_{-d}^{\eta^n} \mathbf{u}^{n+1/2} \, \mathrm{d}z \neq \frac{H^n}{2} \left(\overline{\mathbf{u}}^{n+1} + \overline{\mathbf{u}}^{n} \right) \tag{33}$$

The origin of this discrepancy is partly caused by the inexact separation between the external and internal modes (Killworth et al., 1991; Higdon and de Szoeke, 1997; Griffies et al., 2001). This is due to the nonlinear coupling terms included in $\mathbf{B}$ in Eq. (29). Hence, the three-dimensional horizontal velocity field must be corrected accordingly so that the above inequality becomes an equality (Shchepetkin and McWilliams, 2005; Haidvogel et al., 2007). Only in doing so is the vertical velocity compatible with the free-surface elevation and global tracer conservation consistently ensured (White et al., 2007). As pointed out by Shchepetkin and McWilliams (2005), a split-explicit approach generally precludes both conservation and consistency to be satisfied, which is another reason backing the choice of a single time step since both properties are fulfilled in this way.

In a finite-element context, the correction introduced by Eq. (33) is also a way to circumvent the issue that Eqs (26) and (30) cannot be satisfied simultaneously, unless the bottom is flat. This is so because when this is not the case, the functional spaces chosen for $\mathbf{u}$ and $\bar{\mathbf{u}}$ turn out to be inconsistent in the sense that the depth average of $\mathbf{u}$ does not belong to the space in which $\bar{\mathbf{u}}$ belongs. The correction corrects this discrepancy. It must be emphasized that, because of this reason, a finite-element model that simultanesouly solves for the three-dimensional momentum equations and the free-surface equation is conceptually cleaner and more elegant, though computationally much more expensive. It is, however, an option to keep in mind as computer power will keep increasing.

In the current version of the model, the mesh motion is controlled by the free-surface oscillations only. Since the external and internal modes are splitted, the new free-surface elevation is known prior to computing the three-dimensional fields. A new mesh (at time step $n+1$) can then be built based on the mesh at time step n by translating the nodes vertically, complying with some chosen criterion. To be consistent, the mesh motion at the surface over the time step Δt must be equal to $\eta^{n+1} - \eta^n$ (White et al., 2007). At the bottom, all nodes remain fixed and the mesh velocity vanishes. In the interior of the domain, the mesh motion over a given vertical is linearly distributed, from zero at the bottom to the displacement of the free surface at the top. The mesh velocity at a given node is the ratio of the node displacement to the time step over which this displacement takes place. It is assumed that the mesh velocity is constant over a time step.

3.4 Overall time staggered algorithm

A schematic illustrating the time staggering of the overall algorithm is depicted in Figure (4). The elevation and tracers are known on integer time steps while the velocity is known on half-integer time steps. The mesh geometry

needs to be known on integer time steps only. This follows from the linearization in time of the free-surface equation (30) and the fact that the three-dimensional horizontal velocity field is corrected on a mesh geometry known on an integer time step (see Eq. 33).

To describe the sequence of computations, we will assume that we know the variables at the following steps: $\overline{\mathbf{u}}^n, \eta^n, \mathbf{u}^{n-1/2}, w^{n-1/2}$ and C^n, where C is any passive or active tracer. The mesh geometry is known at steps $n-1$ and n. We will note these geometries $\mathcal{M}^{n-1}$ and $\mathcal{M}^n$, respectively. The overall algorithm is given hereafter.

1. Compute $(\overline{\mathbf{u}}^{n+1}, \eta^{n+1})$ given $(\overline{\mathbf{u}}^n, \eta^n)$ by solving Eqs (29)-(30).
2. Compute $(\mathbf{u}^{n+1/2})$ on $\mathcal{M}^n$ given $(\mathbf{u}^{n-1/2}, w^{n-1/2})$ on $\mathcal{M}^{n-1}$ by solving Eq. (32).
3. Correct $\mathbf{u}^{n+1/2}$ so that the horizontal transport is equal to (31).
4. Compute $w^{n+1/2}$ on geometry $\mathcal{M}^n$ given $u^{n+1/2}$ on the same geometry by solving Eq. (23).
5. Update both geometries. At this point, we have $\mathcal{M}^n$ and $\mathcal{M}^{n+1}$.
6. Compute any tracer C^{n+1} on geometry $\mathcal{M}^{n+1}$ given the tracer C^n and the velocity $(\mathbf{u}^{n+1/2}, w^{n+1/2})$ on geometry $\mathcal{M}^n$.
7. Return to step 1.

The first action undertaken to improve efficiency – namely separating the dynamics into the slow and fast modes while using a single time step – has already been described. Upon inspection of the time-stepping algorithm outlined in the previous section, we may identify five main computational tasks: the fast mode, the horizontal velocity, the vertical velocity, the tracers and updating the mesh geometry. We note N_{2d} the number of two-dimensional triangle vertices and L the number of layers (a mesh containing L layers means that the total number of vertices is $(2L-1) \times N_{2d}$). In a Delaunay two-dimensional mesh, the number of horizontal edges tends to $3N_{2d}$. The overall computational cost of the algorithm may be established in terms of these two variables:

1. The computation of $(\overline{\mathbf{u}}, \eta)$ requires to solve a system of $7N_{2d}$ unknowns. In a number of large-scale applications, it is legitimate to neglect the free-surface elevation in the divergence term of Eq. (28). Hence, the left-hand side matrix of the system is constant in time and need only be factorized once at the onset of the time integration. The direct solver UMFPACK is used (Davis, 2004).
2. The computation of either component of $\mathbf{u}$ requires to solve a system of $2L \times 3N_{2d} = 6LN_{2d}$ unknowns. The factor $2L$ is a consequence of the discontinuous representation in the vertical. Due to the orthogonality of the non-conforming basis functions in the horizontal (Hua and Thomasset, 1984), the left-hand side matrix is banded diagonal, with a bandwidth of two. In the horizontal, a three-point Hammer quadrature rule is used for which integration points are located on the same vertical as that where velocity nodes lie. This ensures horizontal orthogonality. Note that without vertical momentum diffusion (which is implicit in time), the left-hand side of the linear system reduces to a tridiagonal matrix.
3. When solving Eq. (23) for w, we lump the left-hand side matrix of the system in the horizontal to obtain a tridiagonal matrix. The vertical velocity used in the tracer equation must then be modified accordingly in order to remain consistent. The number of unknowns is $2L \times N_{2d} = 2LN_{2d}$ and the computational cost scales like $\mathcal{O}(LN_{2d})$. Note that, although the scaling is the same as that for $\mathbf{u}$, the cost of solving the system for w is roughly 10 times smaller than for either component of $\mathbf{u}$. The reason is that there are three times fewer unknowns for w than for u and v and that a tridiagonal matrix need be factorized for w instead of a banded diagonal matrix for u and v.
4. In case we have a tracer, the number of unknowns is $2L \times N_{2d} = 2LN_{2d}$ and the computational cost scales like $\mathcal{O}(LN_{2d})$ if the left-hand side matrix of the system is lumped horizontally for the vertical diffusion term. Mass lumping, if any, must be performed in all directions for the mass to be conserved.
5. The cost of updating the mesh geometry (i.e., computing the normals, the element Jacobians and the new coordinates) is proportional to the number of elements, which scales like $\mathcal{O}(LN_{2d})$.

Therefore, the overall computational cost of the algorithm scales like $\mathcal{O}(LN_{2d})$. Doubling the number of triangles (i.e., doubling N_{2d}) and doubling the number of layers will quadruple the computational cost. The total number of unknowns (with two tracers) is $18LN_{2d} + 7N_{2d}$.

4 Application to a shallow-water island

Seeking to validate the three-dimensional barotropic component of our model, we opt for a realistic test case. The latter should be three-dimensional (without baroclinic effects) to be able to observe clear vertical motions. The momentum horizontal advection scheme must be severely evaluated, so a problem featuring flow separation and recirculation with formation of eddies is deemed appropriate. Rattray Island (Great Barrier Reef, northeast Australia – Figure 5a) lies perpendicular to tidal currents and stable eddies develop in the wake at rising and falling tides. Rattray Island has been the focus of many studies in the past two decades (Wolanski et al., 1984; Falconer et al., 1986; Black and Gay, 1987; Wolanski and Hamner, 1988; Deleersnijder et al., 1992; Wolanski et al., 1996, 2003; White and Deleersnijder, 2007). Aerial photographs show turbid water in the wake of Rattray Island both at rising and falling tides. This suggests that sediment-laden water is carried upwards to the surface by vertical transport during the life span of the eddies. This is confirmed by backscatterance measurements (White and Wolanski, 2007). In December 1982 (Wolanski et al., 1984), 26 current meters were deployed in the wake of Rattray (Figure 5b), which are used here for validation.

4.1 Model setup

Currents are dominated by the tides, whose ellipses are strongly polarized and oriented from northwest to southeast. The domain is rotated so as to minimize the x-component of the far-field velocity used as boundary condition (Figure 6b). The side boundaries (parallel to the y-axis) are then essentially parallel to the major axis of the tidal ellipses and may be considered impermeable. The southeast and northwest boundaries – hereafter referred to as lower and upper boundaries, respectively – remain open. Using available field measurements, the depth-averaged normal velocity and the elevation are imposed at both the lower and upper boundaries by prescribing the incoming characteristic variable $\bar{u}_n - \eta\sqrt{g/h}$, where $\bar{u}_n$ is the depth-averaged normal velocity (Flather, 1976; Blayo and Debreu, 2005). Either current meter 4 or 25 is used as velocity forcing. The phase lag between both boundaries is less than 20 minutes and is neglected in the model. Forcing used in the model corresponds to a 3.5 m spring tide recorded between 23 November 1982 and 4 December 1982. Rising tide flows southeastward.

Because of the domain's limited extent, the f-plane approximation is made with the latitude being 20°S. The roughness length is taken to be $\xi_0 = 5 \times 10^{-3}$ m in Eq. (10) (Black and Gay, 1987). Because the last velocity node lies on the seabed, the bottom stress (10) is computed by using the mean value of the last two velocity nodes. The distance to the seabed ξ_b is calculated accordingly. We neglect surface stress as there was no significant wind during the field survey (Wolanski et al., 1984). The constant c_s used in the parameterization of the horizontal momentum diffusion coefficient, Eq. (5), is equal to 0.05. This yields maximum values for the momentum diffusion coefficient of about 0.5 m^2 s^{-1}. The two meshes M_1 and M_2 used are shown in Figure 6.

4.2 Model results

All results below are presented on 4 December 1982. This is the only day (with 2 December) for which all current meters were deployed. The flow pattern for a full tidal cycle is presented in Figure 7. The simulation is run on mesh M_2, starting at 1h30 on 4 December and snapshots are shown every two hours. The flow pattern agrees well with previous calculations and observations.

A quantitative model assessment is presented in Table 1 where three model runs are compared. They differ by the mesh used and the current meter chosen as provider of velocity for the boundary condition. Three different RMS (root mean square) errors $\mathcal{E}$ between the measured and numerically predicted depth-averaged horizontal velocities are computed. Each of them corresponds to a given set of current meters considered in the calculation of the RMS error. That is,

$$\mathcal{E} = \left\{ \frac{1}{N} \sum_{i \in S} \left[(u_i^{num} - u_i^{meas})^2 + (v_i^{num} - v_i^{meas})^2 \right] \right\}^{1/2}, \tag{34}$$

where u and v are both velocity components, superscripts *num* and *meas* refer to numerically predicted and measured quantities, respectively and i is the current meter index. The set of N current meters used in the RMS error calculation is noted S, which can be either one of the following

$$S = \begin{cases} \{1, 2, 3, 7, 8, 9, 14, 15, 16, 17\} & \text{for the wake RMS error,} \\ \{18, \ldots, 25\} & \text{for the far-field RMS error,} \\ \{1, \ldots, 25\} & \text{for the global RMS error.} \end{cases}$$

As illustrated in Figure 5b, the wake RMS error considers only those current meters that are under the influence of the island and reached by the eddies. The far-field RMS error considers those current meters that are far enough from the island and are unperturbed by the eddies. The global RMS error uses all current meters. The RMS errors were computed every eight minutes at flood during four hours and during the formation of eddies on the east side of Rattray. Time-mean values are provided in Table 1. Snapshots and model-field comparisons for simulations $S1$-$S3$ are shown in Figures 8-10. Without too much surprise, the finer mesh M_2 provides better predictions in the island's wake, close to Rattray. Comparisons at 12h30 and 13h30 in Figures 8-9 show that the model prediction is much better on the finer mesh for the three current meters closest to the island (current meters 1-3). Now, regardless of the mesh, simulations $S1$ and $S2$ overestimate the flow speed in the far field at 13h30. By using current meter 25 for boundary conditions (see Figure 10), the flow at 13h30 is much better reproduced but the detailed structure of the flow in the vicinity of Rattray has some defects. Depending on which current meter is employed for the boundary condition, RMS errors can thus widely vary. Overall, the far-field current meter 25 yields the lowest global error. The wake RMS error, however, increases when this far-field current meter is used. For a better representation of the wake recirculation patterns, it is best to use current meter 4. At time of tide reversal (close to 13h30 – see bottom panels in Figures 8-10), the far-field velocity is very weak while the eddies are still intense and large. Current meter 4 is under the influence of the persisting eddy and using its data as boundary condition largely overestimates the strength of the far-field velocity. This explains why using current meter 4 as boundary condition yields a much larger far-field RMS error than with current meter 25 (Table 1).

Vertical motions around Rattray Island can be quite intense (reaching a few cm s^{-1} off the island's tips and in the wake), as evidenced by higher water turbidity in the wake (Wolanski et al., 1984, 1996; White and Wolanski, 2007). These vertical motions are of particular concern for marine biologists (e.g., Wolanski and Hamner, 1988; Suthers et al., 2004) and have spurred studies to quantify their intensity (Deleersnijder et al., 1992; White and Deleersnijder, 2007). Here, a passive tracer is used to diagnose these vertical motions over a tidal cycle. The simulation starts with a cylinder-shaped tracer patch, whose horizontal axis is located 20 m below the surface (Figure 11a). In the tracer equation (4), vertical diffusion is turned off so that vertical advection is the only cause for the presence of tracer at the surface. As the tide falls (Figure 11b-c), the cylinder is flushed on the east side of the island but no tracer is found yet at the surface. When the tide rises, the cylinder shifts side and some tracer is found at the surface very close to the island (Figure 11d-e). When tide falls again (Figure 11f), a patch of tracer is clearly visible at the surface, off the southern tip of Rattray. This situation bears many similarities with an aerial photograph (Figure 12 in the paper by Wolanski et al. (1984)) where a patch of turbid water is clearly visible at this location shortly after tide reversal.

This analysis does not take into account the settling and buoyancy of sediments. In that respect, it is incomplete. But, it provides yet another argument in favor of the three-dimensional character of the tidal flow around Rattray Island. This last experiment also provided a test case for the numerical treatment of the tracer equation presented by White et al. (2007).

5 Application to a wind-driven channel

To assess the ability of the model to properly reproduce the vertical structure of the three-dimensional velocity field, we now consider a wind-driven flow experiment similar to that presented by Winant (2004). The domain of interest consists of an elongated rectangular basin. The longitudinal and cross coordinates are noted x and y, respectively (Figure 12). The depth does not depend on the longitudinal coordinate x and is taken to be a smooth function of y (a Gaussian), with maximum depth at the center of the basin and the shallowest part near the longitudinal boundaries. To avoid having to deal with vanishing layers near the longitudinal boundaries, the depth at these boundaries is taken to be a positive constant. Uniform wind is blowing over the water surface in the longitudinal direction.

Equations (1)-(3) are solved with some modifications. The momentum equation is linearized by discarding advection. Horizontal momentum diffusion is discarded but vertical momentum diffusion is kept. Bottom friction is

preserved to dissipate the energy input from the wind. The purpose of this experiment is to verify whether the model is able to represent the vertical structure of the horizontal velocity field, shaped by the combined effects of bottom friction, wind friction and vertical diffusion.

The basin is taken to be 30 km long, 10 km wide and 30 m deep at the center. The wind stress is $||\boldsymbol{\tau}_s|| = 0.1$ N m^{-2}, the coefficient of vertical momentum diffusion is $\nu_z = 5 \times 10^{-4}$ m^2 s^{-1} and the Coriolis factor is $f = 10^{-4}$ s^{-1}. The quadratic law (10) is used with the bottom drag coefficient taken to be 10^{-3}. That is, the drag coefficient is constant and not parameterized. A three-dimensional mesh containing approximately 6500 surface triangles (mean resolution of about 300 m) and 20 layers is used to run the model during 2.9 days with a time step of 500 s.

The predicted flow field is in good agreement with published results by Mathieu et al. (2002) and Winant (2004), as shown in Figure 13. The barotropic transport is upwind (i.e., negative) in the deep part of the basin and downwind (i.e., positive) in the shallow region (see the u-component). However, the surface zonal velocity is everywhere positive, which is a direct effect of wind drag. The vertical structure of the v-component exhibits two co-rotating eddies with negative values near the surface and the bottom and a slow positive returning flow in the interior. These results are in qualitative and quantitative agreement with those published by Winant (2004).

6 Conclusions

We presented a new three-dimensional, unstructured mesh finite element shallow-water model. The current configuration is suitable for studying unstratified flows and the evolution of passive tracers. The model has a free surface and is hydrostatic. The mesh is unstructured in the horizontal and extruded towards the seabed in the direction parallel to the local gravity vector to generate a mesh made up of prisms. The mesh moves in the vertical and accommodates the free-surface motions.

We described the numerical treatment of the hydrodynamical equations with the finite element method. A discontinuous representation is used in the vertical for all velocity components. The horizontal components are nonconforming in the horizontal, which is particularly well suited for advection-dominated flows. The choice of elements (i.e., the nodes stagering) follows the guidelines by White et al. (2007) and is consistent and ensures volume and tracer conservation.

The model was validated against a realistic tidal flow around a shallow-water island for which field measurements are available and was shown to operate successfully. The three-dimensional character of the flow was emphasized by use of a passive tracer for which vertical diffusion was turned off. The presence of tracer at the surface is a signature of vertical motions of relatively high intensity. Finally, we assessed the model's ability to represent the vertical structure of the horizontal flow field by applying it to a wind-driven flow experiment in an elongated rectangular basin.

This three-dimensional shallow-water model is built on several breakthroughs that have been – or are about to be – published and, in this respect, is an important step toward a full-fledged ocean model. Yet, many challenges still lie ahead of us. One of the biggest is the activation of the baroclinic pressure term, which hinges on the adequate transport of active tracers such as temperature and salinity. This, in turn, implies that great care will have to be taken in devising the advection scheme for scalars. The elements chosen in the model for all variables ensure consistency but positive-definiteness of tracer distributions will eventually depend on the advection operator and, to a lesser extent, the diffusion operator (Delhez and Deleersnijder, 2007). As many ocean models are now linked to biogeochemical cycles, the issue of devising a monotonic, positive-definite advection scheme is even more pressing. The model must be able to operate in spherical geometry without resorting to global coordinate systems that present one or more numerical singularities (such as the longitude-latitude coordinate system). Mesh flexibility will be fully exploited in the vertical by using different numbers of prisms within each column. We also must demonstrate that, from a computational point of view, finite element models are a viable alternative to the more efficient structured grid models. One step further in sophistication entails embedding a continuous spectrum of parameterizations within finite element models to comply with variable mesh resolution and the formidable multiscale complexity of ocean flows.

Acknowledgments

Laurent White and Eric Deleersnijder are a honorary Postdoctoral Researcher and a Research associate, respectively, with the Belgian National Fund for Scientific Research (FNRS). The comments and suggestions made by two anonymous reviewers greatly helped improve this manuscript. The present study was carried out within the scope of the project "A second-generation model of the ocean system", which is funded by the *Communauté Française de Belgique*,

as *Actions de Recherche Concertées*, under contract ARC 04/09-316. This work is a contribution to the construction of SLIM, the Second-generation Louvain-la-Neuve Ice-ocean Model (http://www.climate.be/SLIM).

A Definition of Sobolev Spaces $\mathcal{H}^1$ and $\mathcal{L}^2$

The space $\mathcal{L}^2(\Omega)$ contains those functions that are square integrable, i.e.,

$$\mathcal{L}^2(\Omega) = \left\{ f : \int_\Omega |f|^2 \, \mathrm{d}\Omega < \infty \right\}.$$

The space $\mathcal{H}^1(\Omega)$ contains those functions belonging to $\mathcal{L}^2(\Omega)$ and whose first weak derivatives belong to $\mathcal{L}^2(\Omega)$ as well. That is

$$\mathcal{H}^1(\Omega) = \left\{ f \in \mathcal{L}^2(\Omega) : \ \forall i = 1 \ldots d, \ \partial_{x_i} f \in \mathcal{L}^2(\Omega) \right\},$$

where d is the dimension of the space ($d = 3$ for the usual physical space).

B Coupling terms between the external and internal modes

Eq. (27) is spelled out in terms of its $x-$ and $y-$components. For the $x-$component, we have

$$\begin{aligned} \frac{\partial \overline{u}}{\partial t} + \overline{u}\frac{\partial \overline{u}}{\partial x} + \overline{v}\frac{\partial \overline{u}}{\partial y} - f\overline{v} + g\frac{\partial \eta}{\partial x} = \quad & -\frac{1}{H}\frac{\partial}{\partial x}\int_{-d}^{\eta} \tilde{u}\tilde{u} \, \mathrm{d}z - \frac{1}{H}\frac{\partial}{\partial y}\int_{-d}^{\eta} \tilde{v}\tilde{u} \, \mathrm{d}z \\ & + \frac{1}{H}\int_{-d}^{\eta} \boldsymbol{\nabla}\cdot(\nu_h \boldsymbol{\nabla} u) \ \mathrm{d}z + \frac{1}{\rho_0 H}\left(\tau_x^s - \tau_x\right) \end{aligned} \tag{35}$$

while the $y-$component reads

$$\begin{aligned} \frac{\partial \overline{v}}{\partial t} + \overline{u}\frac{\partial \overline{v}}{\partial x} + \overline{v}\frac{\partial \overline{v}}{\partial y} + f\overline{u} + g\frac{\partial \eta}{\partial y} = \quad & -\frac{1}{H}\frac{\partial}{\partial x}\int_{-d}^{\eta} \tilde{u}\tilde{v} \, \mathrm{d}z - \frac{1}{H}\frac{\partial}{\partial y}\int_{-d}^{\eta} \tilde{v}\tilde{v} \, \mathrm{d}z \\ & + \frac{1}{H}\int_{-d}^{\eta} \boldsymbol{\nabla}\cdot(\nu_h \boldsymbol{\nabla} v) \ \mathrm{d}z + \frac{1}{\rho_0 H}\left(\tau_y^s - \tau_y\right). \end{aligned} \tag{36}$$

In Eqs (35) and (36), we have defined

$$\tilde{\mathbf{u}} = \mathbf{u} - \overline{\mathbf{u}},$$

which is the deviation of the velocity relative to the depth-averaged velocity. The terms involving products of those deviations arise from depth-integration of advection terms. The bottom and surface stresses are denoted by $\boldsymbol{\tau}$ and $\boldsymbol{\tau}^s$, respectively. In Eqs (35)-(36), all terms involving the prognostic variables $(\overline{u}, \overline{v})$ can be time stepped. The momentum diffusion term is purposedly written in terms of the full velocity field. Only when writing the variational statement of Eqs (35)-(36) are we able to elegantly derive expressions involving the depth-averaged and deviatory velocity components. It is carried out below. Upon inspection of Eqs (35)-(36), we see that the right-hand side $\mathbf{B}$ of Eq. (27) is

$$\begin{aligned} \mathbf{B} = \quad & -\overline{u}\frac{\partial \overline{\mathbf{u}}}{\partial x} - \overline{v}\frac{\partial \overline{\mathbf{u}}}{\partial y} - \frac{1}{H}\frac{\partial}{\partial x}\int_{-d}^{\eta} \tilde{u}\tilde{\mathbf{u}} \, \mathrm{d}z - \frac{1}{H}\frac{\partial}{\partial y}\int_{-d}^{\eta} \tilde{v}\tilde{\mathbf{u}} \, \mathrm{d}z \\ & + \frac{1}{H}\int_{-d}^{\eta} \boldsymbol{\nabla}\cdot(\nu_h \boldsymbol{\nabla}\mathbf{u}) \ \mathrm{d}z + \frac{1}{\rho_0 H}\left(\boldsymbol{\tau}^s - \boldsymbol{\tau}\right). \end{aligned} \tag{37}$$

Let us now focus on the momentum diffusion term in the variational statement associated with Eq. (35). After multiplying the equation by a two-dimensional test function $\hat{u}$ and integrating over the unperturbed, two-dimensional domain $\mathcal{T}^h$, we obtain

$$\begin{aligned} \int_{\mathcal{T}^h} \frac{\hat{u}}{H}\int_{-d}^{\eta} \boldsymbol{\nabla}\cdot(\nu_h \boldsymbol{\nabla} u) \ \mathrm{d}z \, \mathrm{d}\tau = \quad & -\int_{\mathcal{T}^h} \boldsymbol{\nabla}\left(\frac{\hat{u}}{H}\right)\cdot(H\nu_h \boldsymbol{\nabla}\overline{u}) \ \mathrm{d}\tau \\ & -\int_{\Omega^h} \boldsymbol{\nabla}\hat{u}\cdot(\nu_h \boldsymbol{\nabla}\tilde{u}) \ \mathrm{d}\Omega \\ & +\int_{\Omega^h} \frac{\hat{u}}{H^2}\boldsymbol{\nabla}H\cdot(\nu_h \boldsymbol{\nabla}\tilde{u}) \ \mathrm{d}\Omega. \end{aligned} \tag{38}$$

In Eq. (38), the first term in the left-hand side can be time stepped because it is expressed in terms of the prognostic variable $\overline{u}$. In that case, the term dissipates depth-averaged horizontal momentum.

References

Adcroft, A. and Campin, J.-M. (2004). Rescaled height coordinates for accurate representation of free-surface flows in ocean circulation models. *Ocean Model.*, 7:267–284.

Adcroft, A. and Hallberg, R. (2006). On methods for solving the oceanic equations of motion in generalized vertical coordinates. *Ocean Model.*, 11:224–233.

Akin, J. E., Tezduyar, T., Ungor, M., and Mittal, S. (2003). Stabilization parameters and Smagorinsky turbulence model. *Journal of Applied Mechanics*, 70(1):1–9.

Ballantyne, V. A., Foreman, M. G. G., and Jacques, W. R. C. R. (1996). Three-dimensional model simulations for the north coast of British Columbia. *Cont. Shelf Res.*, 16:1655–1682.

Bilgili, A., Smith, K. W., and Lynch, D. R. (2006). BatTri: a two-dimensional bathymetry-based unstructuredtriangular grid generator for finite element circulationmodeling. *Comput. Geosci.*, 32(5):632–642.

Black, K. P. and Gay, S. L. (1987). Eddy formation in unsteday flows. *J. Geophys. Res.*, 92(C9):9514–9522.

Blaise, S., Deleersnijder, E., White, L., and Remacle, J.-F. (2007). Influence of the turbulence closure scheme on the finite-element simulation of the upwelling in the wake of a shallow-water island. *Cont. Shelf Res.*, 27(18):2329–2345.

Blayo, E. and Debreu, L. (2005). Revisiting open boundary conditions from the point of view of characteristic variables. *Ocean Model.*, 9:231–252.

Blumberg, A. F. and Mellor, G. L. (1987). A description of a three-dimensional coastal ocean circulation model. In Heaps, N. S., editor, *Three-Dimensional Coastal Ocean Models*, volume 4, pages 1–16. American Geophysical Union.

Casulli, V. and Walters, R. A. (2000). An unstructured grid, three-dimensional model based on the shallow-water equations. *Int. J. Numer. Methods Fluids*, 32(3):331–346.

Chen, C., Liu, H., and Beardsley, R. C. (2003). An unstructured grid, finite-volume, three-dimensional, primitive equations ocean model: application to coastal ocean and estuaries. *J. Atmos. Ocean. Technol.*, 20:159–186.

Cushman-Roisin, B. and Naimie, C. E. (2002). A 3D finite-element model of the Adriatic tides. *J. Mar. Syst.*, 37(4):279–297.

Danilov, S., Kivman, G., and Schröter, J. (2004). A finite-element ocean model: principles and evaluation. *Ocean Model.*, 6:125–150.

Danilov, S., Kivman, G., and Schröter, J. (2005). Evaluation of an eddy-permitting finite-element ocean model in the North Atlantic. *Ocean Model.*, 10:35–49.

Davis, T. A. (2004). A column pre-ordering strategy for the unsymmetric-pattern multifrontal method. *ACM Transactions on Mathematical Software*, 30:165–195.

Dawson, C., Westerink, J. J., Feyen, J. C., and Pothina, D. (2006). Continuous, discontinuous and coupled discontinuous-continuous Galerkin finite element methods for the shallow water equations. *Int. J. Numer. Methods Fluids*, 52:63–88.

Deleersnijder, E., Norro, A., and Wolanski, E. (1992). A three-dimensional model of the water circulation around an island in shallow water. *Cont. Shelf Res.*, 12(7/8):891–906.

Deleersnijder, E. and Ruddick, K. G. (1989). A generalized vertical coordinate for 3D marine models. *Bulletin de la Société Royale des Sciences de Liège*, 61(6):489–502.

Delhez, E. J. and Deleersnijder, E. (2007). Overshootings and spurious oscillations caused by biharmonic mixing. *Ocean Model.*, 17:183–198.

Dukowicz, J. K. and Smith, R. D. (1994). Implicit free-surface method for the Bryan-Cox-Semtner ocean model. *J. Geophys. Res.*, 99(4):7991–8014.

Falconer, R. A., Wolanski, E., and Mardapitta-Hadjipandeli, L. (1986). Modeling tidal circulation in an island's wake. *J. Waterw. Port Coast. Ocean Eng.-ASCE*, 112:234–254.

Fischer, H. B., List, E. Y., Koh, R. C. Y., Imberger, J., and Brooks, N. H. (1979). *Mixing in inland and coastal waters*. Academic Press, New York.

Fix, G. J. (1975). Finite element models for ocean circulation problems. *SIAM J. Appl. Math.*, 29:371–387.

Flather, R. A. (1976). A tidal model of the northwest European continental shelf. *Mémoires de la Société Royale des Sciences de Liège*, 6(10):141–164.

Ford, R., Pain, C. C., Piggott, M. D., Goddard, A. J. H., de Oliveira, C. R. E., and Umpleby, A. P. (2004a). A non-hydrostatic finite element model for three-dimensional stratified oceanic flows. Part I: model formulation. *Mon. Wea. Rev.*, 132:2816–2831.

Ford, R., Pain, C. C., Piggott, M. D., Goddard, A. J. H., de Oliveira, C. R. E., and Umpleby, A. P. (2004b). A non-hydrostatic finite element model for three-dimensional stratified oceanic flows. Part II: model validation. *Mon. Wea. Rev.*, 132:2832–2844.

Foreman, M. G. G., Walters, R. A., andC. P. Keller, R. F. H., and Dolling, A. G. (1995). A tidal model for the eastern Juan de Fuca Strait and the southern Strait of Georgia. *J. Geophys. Res.*, 100(C1):721–740.

Formaggia, L. and Nobile, F. (2004). Stability analysis of second-order time accurate schemes for ALE-FEM. *Comput. Meth. Appl. Mech. Eng.*, 193:4097–4116.

Fortunato, A. B., Baptista, A. M., and Luettich, R. A. (1997). A three-dimensional model of tidal currents in the mouth of the Tagus estuary. *Cont. Shelf Res.*, 17(14):1689–1714.

Fringer, O. B., Gerritsen, M., and Street, R. L. (2006). An unstructured-grid, finite-volume, non hydrostatic, parallel coastal ocean simulator. *Ocean Model.*, 14:139–173.

Gerdes, R. (1993). A primitive equation ocean circulation model using a general vertical coordinate transformation 1. Description and testing of the model. *J. Geophys. Res.*, 98(C8):14683–14701.

Greenberg, D. A., Dupont, F., Lyard, F. H., Lynch, D. R., and Werner, F. E. (2007). Resolution issues in numerical models of oceanic and coastal circulation. *Cont. Shelf Res.*, 27:1317–1343.

Greenberg, D. A., Werner, F. E., and Lynch, D. R. (1998). A diagnostic finite element ocean circulation model in spherical-polar coordinates. *J. Atmos. Ocean. Technol.*, 15:942–958.

Griffies, S. M. (2004). *Fundamentals of Ocean Climate Models*. Princeton University Press, Princeton (New Jersey).

Griffies, S. M., Böning, C., Bryan, F. O., Chassignet, E. P., Gerdes, R., Hasumi, H., Hirst, A., A.-M.Treguier, and Webb, D. (2000). Developments in ocean climate modelling. *Ocean Model.*, 2:123–192.

Griffies, S. M. and Hallberg, R. W. (2000). Biharmonic friction with a Smagorinsky-like viscosity for use in large-scale eddy-permitting ocean models. *Mon. Wea. Rev.*, 128:2935–2946.

Griffies, S. M., Pacanowski, R. C., Schmidt, M., and Balah, V. (2001). Tracer conservation with an explicit free surface method for z-coordinate ocean models. *Mon. Wea. Rev.*, 129:1081–1098.

Haidvogel, D., Arango, H., Budgell, W., Cornuelle, B., Curchitser, E., Lorenzo, E. D., Fennel, K., Geyer, W., Hermann, A., Lanerolle, L., Levin, J., McWilliams, J., Miller, A., Moore, A., Powell, T., Shchepetkin, A., Sherwood, C., Signell, R., Warner, J., and Wilkin, J. (2007). Ocean forecasting in terrain-following coordinates: formulation and skill assessment of the Regional Ocean Modeling System. *J. Comput. Phys.* in press.

Haidvogel, D. B., Curchitser, E., Iskandarani, M., Hughes, R., and Taylor, M. A. (1997). Global modeling of the ocean and atmosphere using the spectral element method. *Atmos. Ocean*, 35:505–531.

Ham, D. A., Pietrzak, J., and Stelling, G. S. (2005). A scalable unstructured grid 3-dimensional finite volume model for the shallow water equations. *Ocean Model.*, 10:153–169.

Hanert, E., Deleersnijder, E., and Legat, V. (2006). An adaptive finite element water column model using the Mellor-Yamada level 2.5 turbulence closure scheme. *Ocean Model.*, 12:205–223.

Hanert, E., Le Roux, D. Y., Legat, V., and Deleersnijder, E. (2004). Advection shemes for unstructured grid ocean modelling. *Ocean Model.*, 7:39–58.

Hanert, E., Le Roux, D. Y., Legat, V., and Deleersnijder, E. (2005). An efficient Eulerian finite element method for the shallow water equations. *Ocean Model.*, 10:115–136.

Hanert, E., Legat, V., and Deleersnijder, E. (2003). A comparison of three finite elements to solve the linear shallow water equations. *Ocean Model.*, 5:17–35.

Higdon, R. L. and de Szoeke, R. A. (1997). Barotropic-baroclinic time splitting for ocean circulation modeling. *J. Comput. Phys.*, 135:30–53.

Houston, P., Schwab, C., and Süli, A. (2002). Discontinuous hp-finite element methods for advection-diffusion-reaction problems. *SIAM J. Numer. Anal.*, 39(6):2133–2163.

Hua, B.-L. and Thomasset, F. (1984). A noise-free finite element scheme for the two-layer shallow water equations. *Tellus Ser. A*, 36:157–165.

Ingram, R. G. and Chu, V. H. (1987). Flow around islands in Ruppert Bay: an investigation of the bottom friction effect. *J. Geophys. Res.*, 92(C13):14,521–14,533.

Iskandarani, M., Haidvogel, D. B., and Levin, J. C. (2003). A three-dimensional spectral element model for the solution of the hydrostatic primitive equations. *J. Comput. Phys.*, 186:397–425.

Iskandarani, M., Levin, J. C., Choi, B.-J., and Haidvogel, D. B. (2005). Comparison of advection schemes for high-order h-p finite element and finite volume methods. *Ocean Model.*, 10:51–67.

Kasahara, A. (1974). Various vertical coordinate systems used for numerical weather predictions. *Mon. Wea. Rev.*, 102:509–522.

Killworth, P. D., Stainforth, D., Webb, D. J., and Paterson, S. M. (1991). The development of a free-surface Bryan-Cox-Semtner ocean model. *J. Phys. Oceanogr.*, 21:1333–1348.

Kinnmark, I. (1986). *The Shallow Water Wave Equations: Formulation, Analysis and Applications*, volume 15 of *Lecture Notes in Engineering*. Springer-Verlag.

Kolar, R. L., Westerink, J. J., Cantekin, M. E., and Blain, C. (1994). Aspects of nonlinear simulations using shallow-water models based on the wave continuity equation. *Comput. Fluids*, 23(3):523–538.

Le Provost, C., Genco, M.-L., and Lyard, F. (1995). Modeling and predicting tides over the World Ocean. In Lynch, D. R. and Davies, A. M., editors, *Quantitative skill assessment for coastal ocean models*, volume 47 of *Coastal and Estuarine Series*, pages 175–201. American Geophysical Union.

Le Roux, D. Y. (2005). Dispersion relation analysis of the $P_1^{NC} - P_1$ finite-element pair in shallow-water models. *SIAM J. Sci. Comput.*, 27(2):394–414.

Le Roux, D. Y., Lin, C. A., and Staniforth, A. (2000). A semi-implicit semi-lagrangian finite element shallow-water ocean model. *Mon. Wea. Rev.*, 128:1384–1401.

Le Roux, D. Y., Sène, A., Rostand, V., and Hanert, E. (2005). On some spurious mode issues in shallow-water models using a linear algebra approach. *Ocean Model.*, 10:83–94.

Le Roux, D. Y., Staniforth, A., and Lin, C. A. (1998). Finite elements for shallow-water equation ocean models. *Mon. Wea. Rev.*, 126:1931–1951.

Legrand, S., Deleersnijder, E., Delhez, E., and Legat, V. (2007). Unstructured, anisotropic mesh generation for the Northwestern European continental shelf, the continental slope and the neighboring ocean. *Cont. Shelf Res.*, 27:1344–1356.

Legrand, S., Deleersnijder, E., Hanert, E., Legat, V., and Wolanski, E. (2006). High-resolution unstructured meshes for hydrodynamic models of the Great Barrier Reef, Australia. *Estuar. Coast. Shelf Sci.*, 68:36–46.

Legrand, S., Legat, V., and Deleersnijder, E. (2000). Delaunay mesh generation for an unstructured-grid ocean general circulation model. *Ocean Model.*, 2:17–28.

Levin, J. C., Iskandarani, M., and Haidvogel, D. B. (2006). To continue or discontinue: Comparison of continuous and discontinuous Galerkin formulations in a spectral element ocean model. *Ocean Model.*, 15:56–70.

Luettich, R. A. and Westerink, J. J. (1995). Continental shelf scale convergence studies with barotropic tidal model. In Lynch, D. R. and Davies, A. M., editors, *Quantitative skill assessment for coastal ocean models*, volume 47 of *Coastal and Estuarine Series*, pages 349–371. American Geophysical Union.

Lynch, D. R. and Gray, W. R. (1979). A wave equation model for finite element tidal computations. *Comput. Fluids*, 7:207–228.

Lynch, D. R., Ip, J. T. C., Naimie, C. E., and Werner, F. E. (1996). Comprehensive coastal circulation model with application to the Gulf of Maine. *Cont. Shelf Res.*, 16:875–906.

Lynch, D. R. and Werner, F. E. (1987). Three-dimensional hydrodynamics on finite elements. Part I: linearized harmonic model. *Int. J. Numer. Methods Fluids*, 7:871–909.

Lynch, D. R. and Werner, F. E. (1991). Three-dimensional hydrodynamics on finite elements. Part II: non-linear time-stepping model. *Int. J. Numer. Methods Fluids*, 12:507–533.

Massey, T. C. and Blain, C. A. (2006). In search of a consistent and conservative mass flux for the GWCE. *Comput. Meth. Appl. Mech. Eng.*, 195:571–587.

Mathieu, P.-P., Deleersnijder, E., Cushman-Roisin, B., Beckers, J.-M., and Bolding, K. (2002). The role of topography in small well-mixed bays, with application to the lagoon of mururoa. *Cont. Shelf Res.*, 22:1379–1395.

Myers, P. G. and Weaver, A. J. (1995). A diagnostic barotropic finite-element ocean circulation model. *J. Atmos. Ocean. Technol.*, 12:511–526.

Nechaev, D., Schröter, J., and Yaremchuk, M. (2003). A diagnostic stabilized finite-element ocean circulation model. *Ocean Model.*, 5:37–63.

Pain, C. C., Piggott, M. D., Goddard, A. J. H., Fang, F., Gorman, G. J., Marshall, D. P., Eaton, M. D., Power, P., and de Oliveira, C. R. E. (2005). Three-dimensional unstructured mesh ocean modelling. *Ocean Model.*, 10:5–33.

Pietrzak, J., Deleersnijder, E., and Schröter, J., editors (2005). *The Second International Workshop on Unstructured Mesh Numerical Modelling of Coastal, Shelf and Ocean Flows*, volume 10 of *Ocean Model.* Elsevier.

Pietrzak, J., Iskandarani, M., Schröter, J., and Lyard, F., editors (2006). *The Third International Workshop on Unstructured Mesh Numerical Modelling of Coastal, Shelf and Ocean Flows*, volume 15 of *Ocean Model.* Elsevier.

Piggott, M. D., Pain, C. C., Gorman, G. J., Power, P. W., and Goddard, A. J. H. (2005). h, r, and hr adaptivity with applications in numerical ocean modelling. *Ocean Model.*, 10:95–113.

Shchepetkin, A. F. and McWilliams, J. C. (2005). The regional oceanic modeling system (ROMS): a split-explicit, free-surface, topography-following-coordinate oceanic model. *Ocean Model.*, 9:347–404.

Simons, T. J. (1974). Verification of numerical models of Lake Ontario: Part I. Circulation in spring and early summer. *J. Phys. Oceanogr.*, 4(4):507–523.

Smagorinsky, J. (1963). General circulation experiments with the primitive equations. 1 The basic experiment. *Mon. Wea. Rev.*, 91(5):99–165.

Song, Y. T. and Hou, T. Y. (2006). Parametric vertical coordinate formulation for multiscale, Boussinesq, and non-Boussinesq ocean modelling. *Ocean Model.*, 11:298–332.

Stuhne, G. R. and Peltier, W. R. (2006). A robust unstructured grid discretization for 3-dimensional hydrostatic flows in spherical geometry: A new numerical structure for ocean general circulation modeling. *J. Comput. Phys.*, 213:704–729.

Suthers, I. M., Taggart, C. T., Kelley, D., Rissik, D., and Middleton, J. H. (2004). Entrainment and advection in an island's tidal wake, as revealed by light attenuance, zooplankton, and ichthyoplankton. *Limnol. Oceanogr.*, 49:283–296.

Tomczak, M. (1988). Island wakes in deep and shallow water. *J. Geophys. Res.*, 93(C5):5153–5154.

Walters, R. A. (1992). A three-dimensional, finite element model for coastal and estuarine circulation. *Cont. Shelf Res.*, 12:83–102.

Walters, R. A. (2005). Coastal ocean models: two useful finite element methods. *Cont. Shelf Res.*, 25:775–793.

Walters, R. A. (2006). Design considerations for a finite element coastal ocean model. *Ocean Model.*, 15:90–100.

Walters, R. A. and Werner, F. E. (1989). A comparison of two finite element models of tidal hydrodynamics using the North Sea data set. *Adv. Water Resour.*, 12:184–193.

White, L., Beckers, J.-M., Deleersnijder, E., and Legat, V. (2006a). Comparison between free-surface and rigid-lid finite element models of barotropic instabilities. *Ocean Dynamics*, 56:86–103.

White, L. and Deleersnijder, E. (2007). Diagnoses of vertical transport in a three-dimensional finite-element model of the tidal circulation around an island. *Estuar. Coast. Shelf Sci.*, 74:655–669.

White, L., Legat, V., and Deleersnijder, E. (2007). Tracer conservation for three-dimensional, finite element, free-surface, ocean modeling on moving prismatic meshes. *Mon. Wea. Rev.* in press.

White, L., Legat, V., Deleersnijder, E., and Le Roux, D. (2006b). A one-dimensional benchmark for the propagation of Poincaré waves. *Ocean Model.*, 15:101–123.

White, L. and Wolanski, E. (2007). Flow separation and vertical motions in a tidal flow interacting with a shallow-water island. *Estuar. Coast. Shelf Sci.* in press.

Winant, C. D. (2004). Three-dimensional wind-driven flow in an elongated, rotating basin. *J. Phys. Oceanogr.*, 34:462–476.

Wolanski, E., Asaeda, T., Tanaka, A., and Deleersnijder, E. (1996). Three-dimensional island wakes in the field, laboratory experiments and numerical models. *Cont. Shelf Res.*, 16(11):1437–1452.

Wolanski, E., Brinkman, R., Spagnol, S., McAllister, F., Steinberg, C., Skirving, W., and Deleersnijder, E. (2003). Merging scales in models of water circulation: perspectives from the Great Barrier Reef. In Lakhan, V. C., editor, *Advances in Coastal Modeling*, volume 67 of *Elsevier Oceanography Series*, chapter 15, pages 411–429. Elsevier Science.

Wolanski, E. and Hamner, W. M. (1988). Topographically controlled fronts in the ocean and their biological influence. *Science*, 241(4862):177–181.

Wolanski, E., Imberger, J., and Heron, M. L. (1984). Island wakes in shallow coastal waters. *J. Geophys. Res.*, 89(C6):10,553–10,569.

List of Figures

Simulation	Mesh	BC	Global RMS error	Wake RMS error	Far-field RMS error
S_1 (Fig. 8)	$M_1 \times 6$	meter 4	0.5239	0.5917	0.7720
S_2 (Fig. 9)	$M_2 \times 10$	meter 4	0.4974	0.5259	0.7533
S_3 (Fig. 10)	$M_2 \times 10$	meter 25	0.4318	0.6125	0.3235

Table 1: Global, wake and far-field rms errors [m s^{-1}] for three different simulations. The simulations are illustrated in Figures 8, 9 and 10. The errors are computed every eight minutes during four hours at flood (see snaphots in Figures 8, 9 and 10) when eddies develop in the wake. In the *Mesh* column, the horizontal mesh and the number of layers are specified. The global rms error is computed by using all current meters while the wake and far-field rms errors are computed by using subsets of all current meters, as shown in Figure 5.

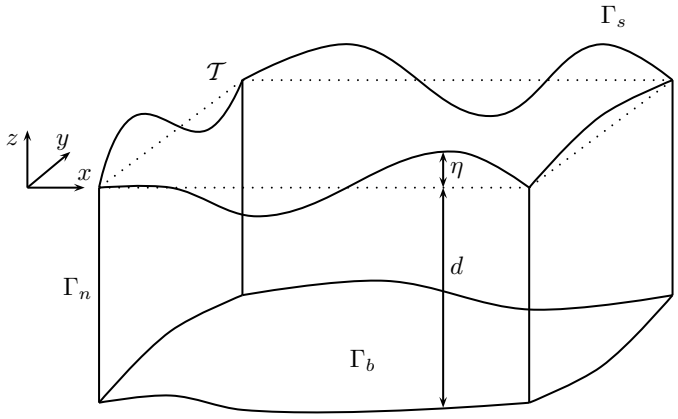

Figure 1: Notations used to describe the three-dimensional time-dependent domain Ω. The seabed and the free surface are denoted by Γ_b and Γ_s, respectively. The unperturbed plane defined by $z = 0$ is noted $\mathcal{T}$ and is represented by the dotted lines. The lateral boundary is noted Γ_n. At any location (x, y), the depth $d(x, y)$ and the elevation $\eta(x, y, t)$ are both defined with reference to $\mathcal{T}$. The displacement of the free surface is exaggerated.

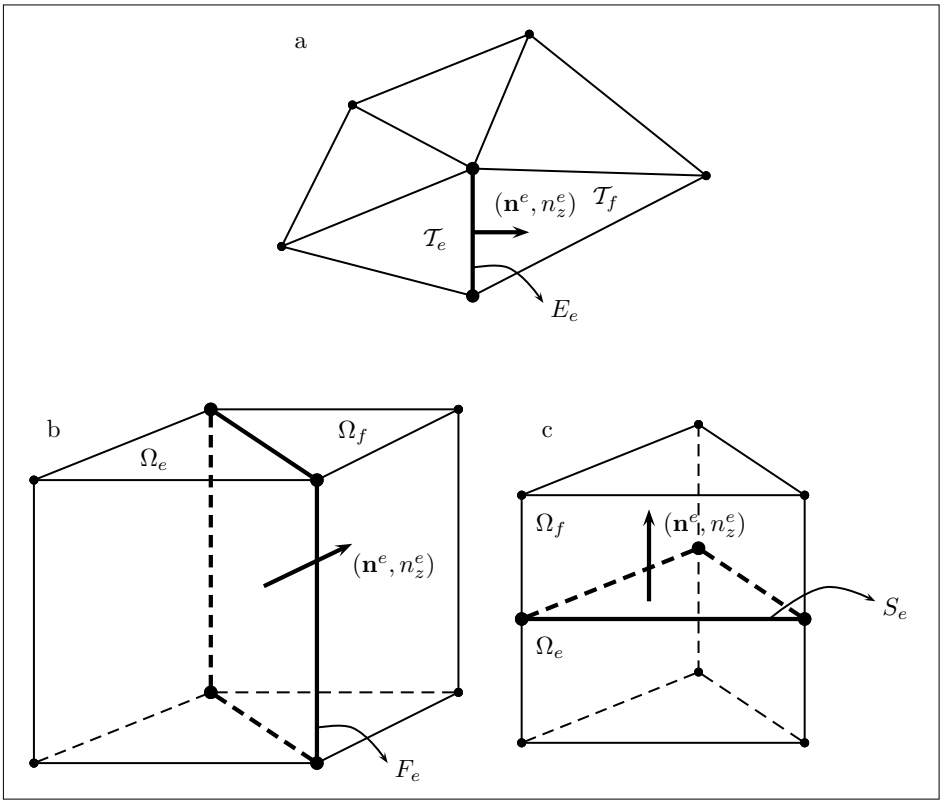

Figure 2: Main notations used to describe the mesh topology. (a) In two dimensions, any interior edge E_e is shared by two triangles $\mathcal{T}_e$ and $\mathcal{T}_f$. In three dimensions, (b) any interior vertical face F_e is common to adjacent prisms Ω_e and Ω_f (lying within a common layer). (c) Two stacked prisms Ω_e and Ω_f share an interior triangular face S_e. A unit normal vector $(\mathbf{n}^e, n_z^e)$ is associated to each of these interior geometric items, with the superscript e indicating that it is oriented from e to f (with $e > f$).

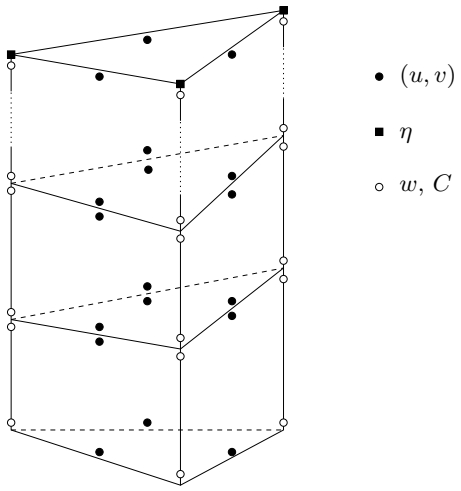

Figure 3: Location of nodes for all hydrodynamic variables within a column split into prisms. The top triangle is the surface triangle. The free-surface elevation (η) is linear. The horizontal velocity (u, v) is linear non-conforming in the horizontal and linear discontinuous in the vertical. The vertical velocity (w) and all tracers (C) are linear everywhere but discontinuous in the vertical.

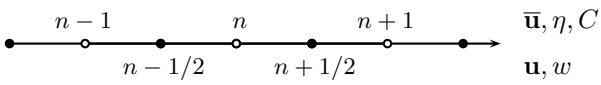

Figure 4: Schematic of the staggering used between elevation and tracers (on integer time steps) and velocity (on half-integer time steps). The mesh geometry needs to be known on integer time steps only, which is a consequence of the transport computed by Eq. (30) not being formally centered in time. The effect is that the velocity $(\mathbf{u}, w)^{n+1/2}$ is computed on mesh geometry n. The symbol C denotes any active or passive tracer.

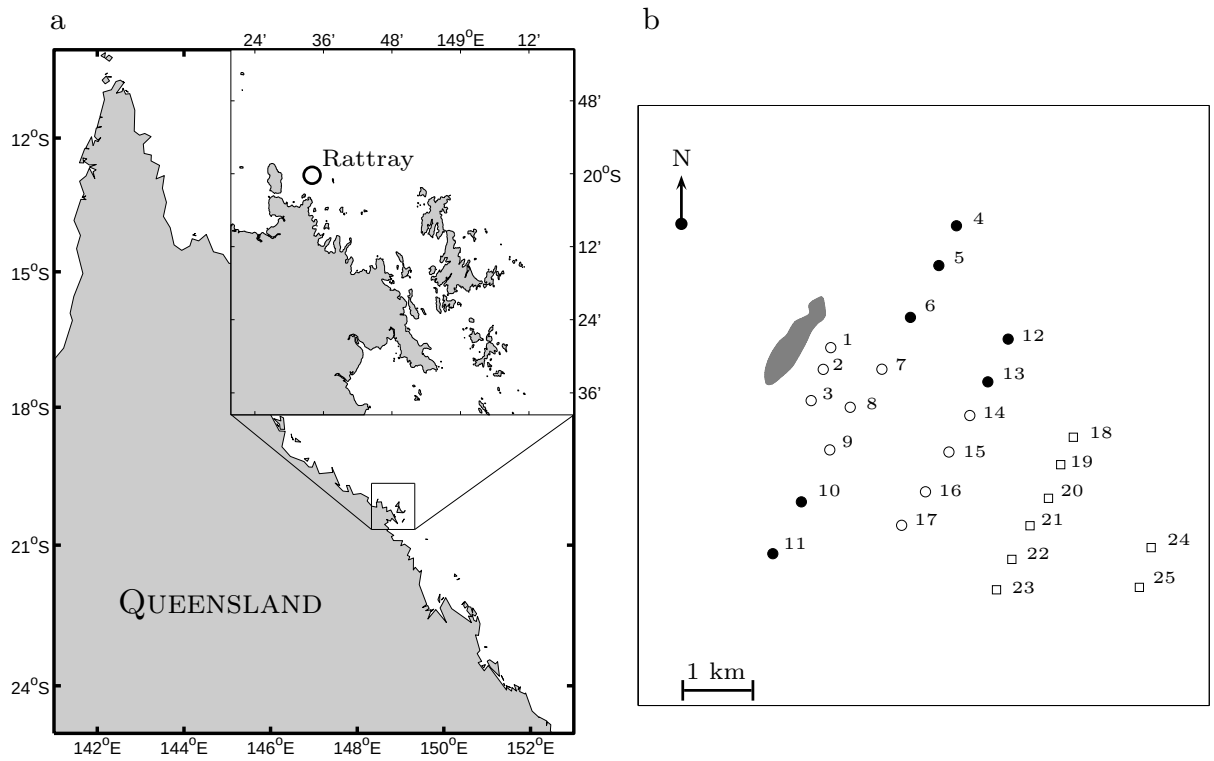

Figure 5: (a) Rattray Island is located in the Great Barrier Reef (northeast Australia). (b) Location and numbering of current meters. Empty circles and squares represent *wake* and *far-field* current meters, respectively. The remaining current meters are represented by filled circles.

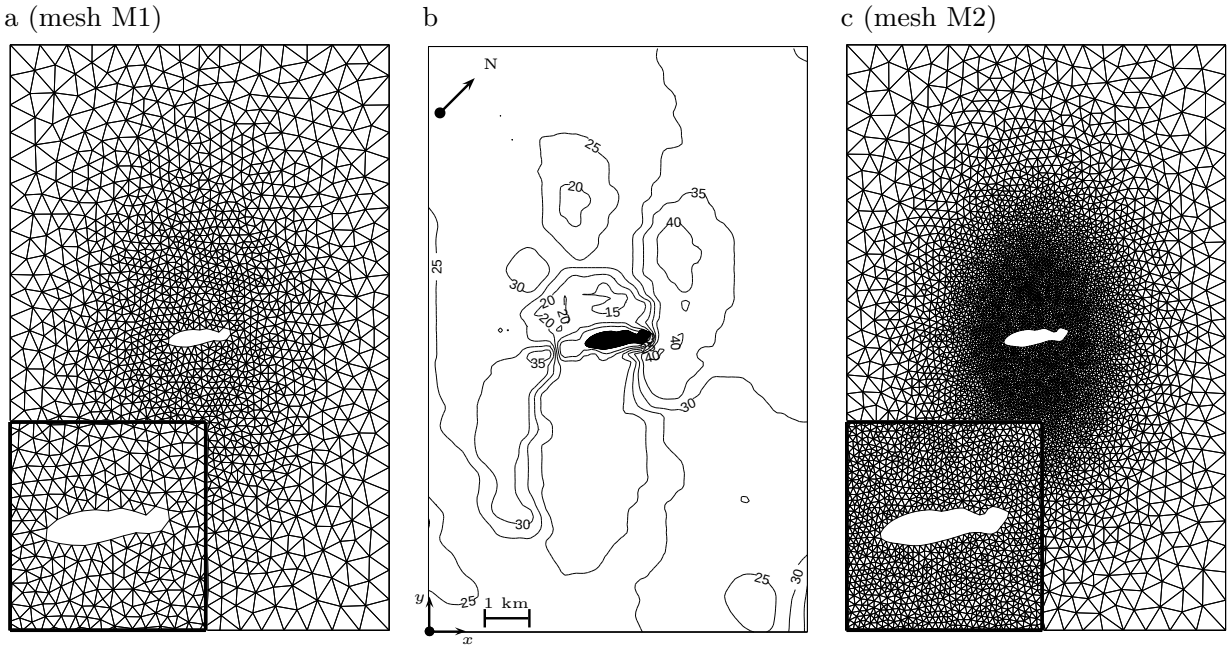

Figure 6: Meshes and bathymetry used in numerical experiments. (a) The horizontal mesh contains 3000 triangles and the resolution varies from 140 m to 900 m. (b) Computational domain (8 km by 11.8 km) and bathymetry, obtained by rotating the real domain by an angle minimizing the x-component of the velocity (in the new coordinate system) used as boundary conditions. (c) The horizontal mesh contains 9600 triangles and the resolution varies from 60 m to 800 m.

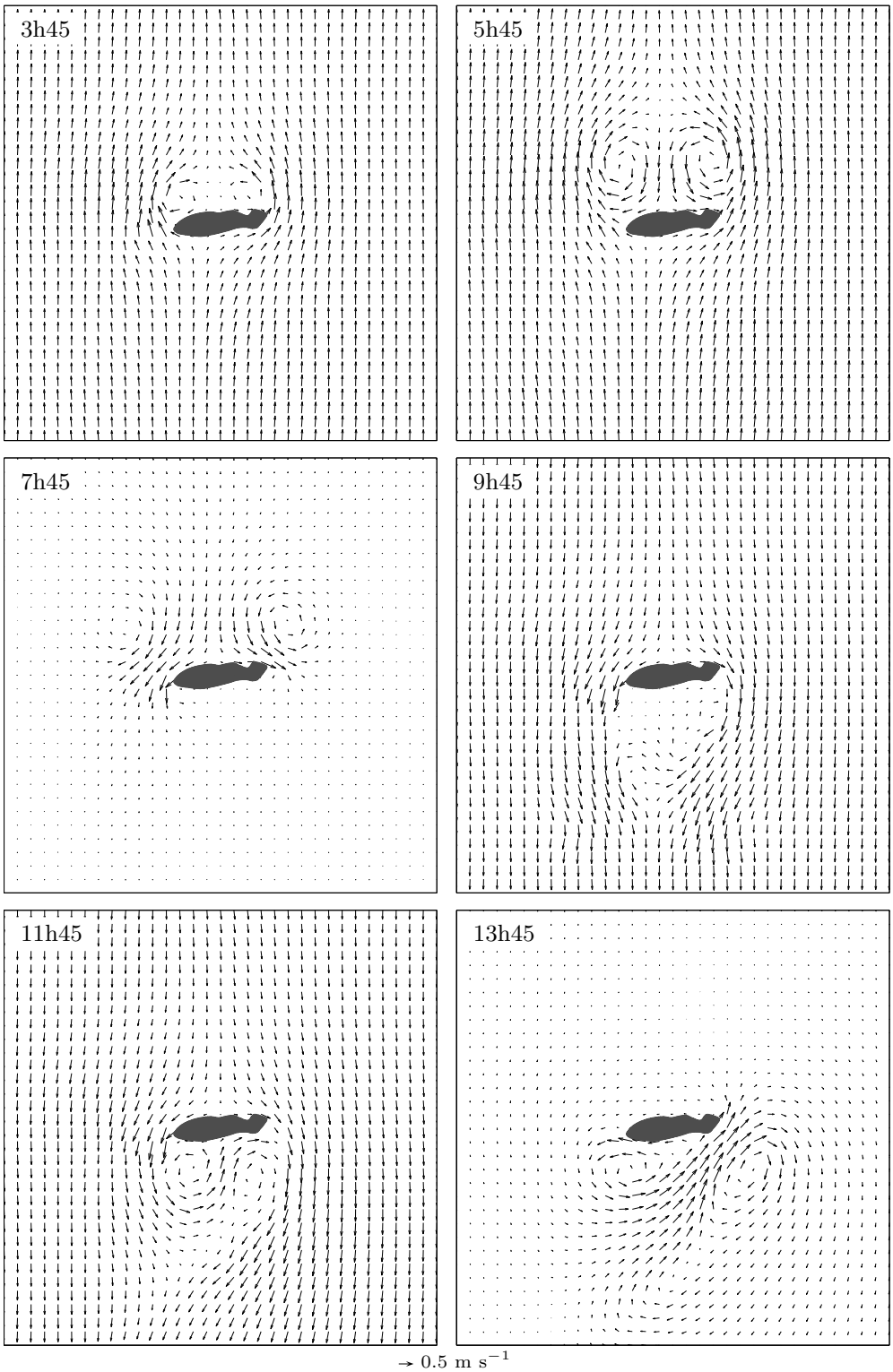

Figure 7: Depth-averaged, horizontal flow pattern at six snapshots during a full tidal cycle. The velocity field was interpolated on a 200 m structured grid for clarity. Velocity from current meter 25 used as open boundary condition. The mesh M_2 was used.

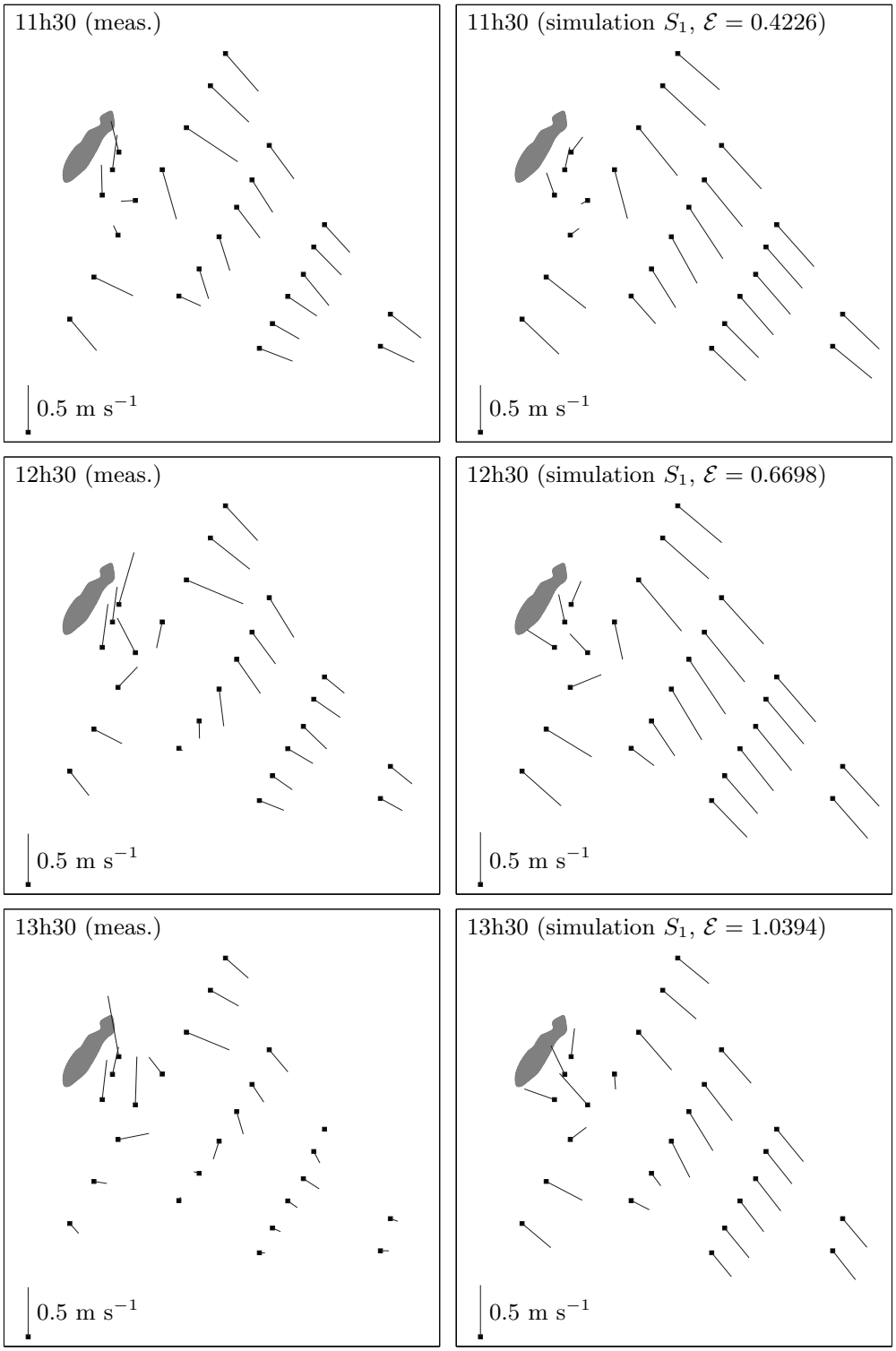

Figure 8: Simulation S_1 (see Table 1). Comparison between the measured depth-averaged horizontal velocity field (left panels) and that predicted by the model (right panels) on 4 December 1982. Tide reversal occurs around 13h45. The rms error $\mathcal{E}$ is computed for each snapshot separately.

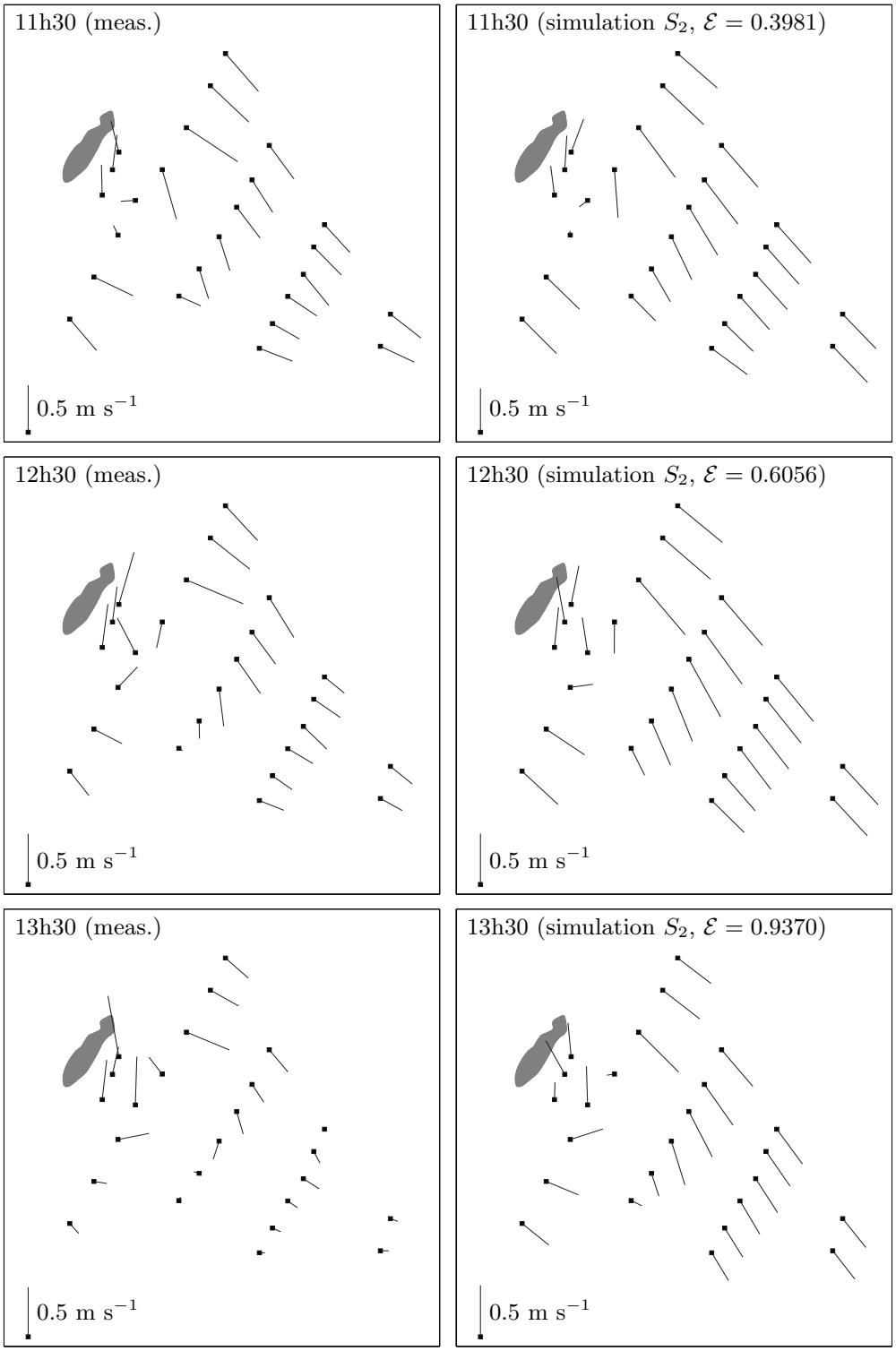

Figure 9: Simulation S_2 (see Table 1). Comparison between the measured depth-averaged horizontal velocity field (left panels) and that predicted by the model (right panels) on 4 December 1982. Tide reversal occurs around 13h45. The rms error $\mathcal{E}$ is computed for each snapshot separately.

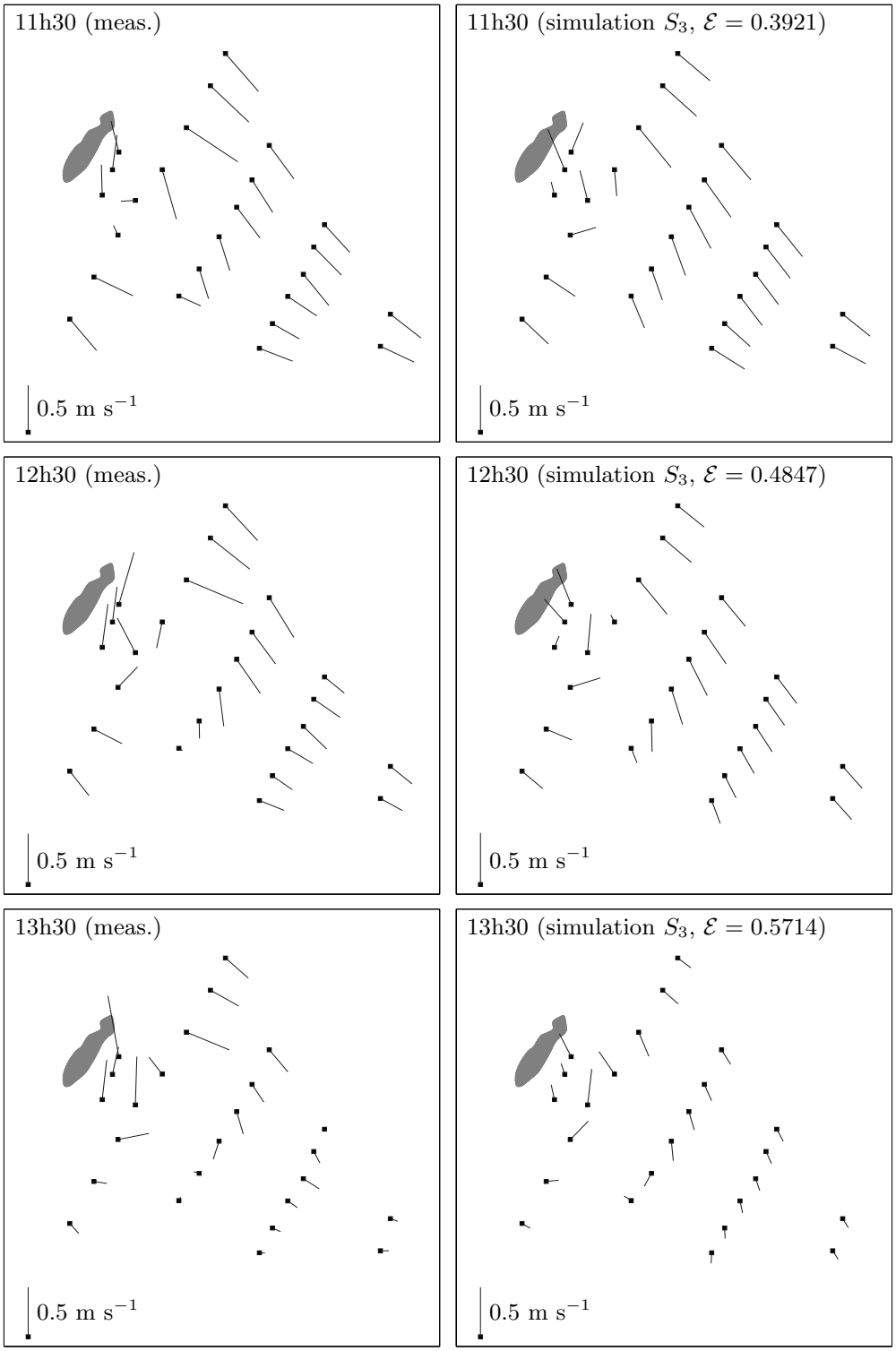

Figure 10: Simulation S_3 (see Table 1). Comparison between the measured depth-averaged horizontal velocity field (left panels) and that predicted by the model (right panels) on 4 December 1982. Tide reversal occurs around 13h45. The rms error $\mathcal{E}$ is computed for each snapshot separately.

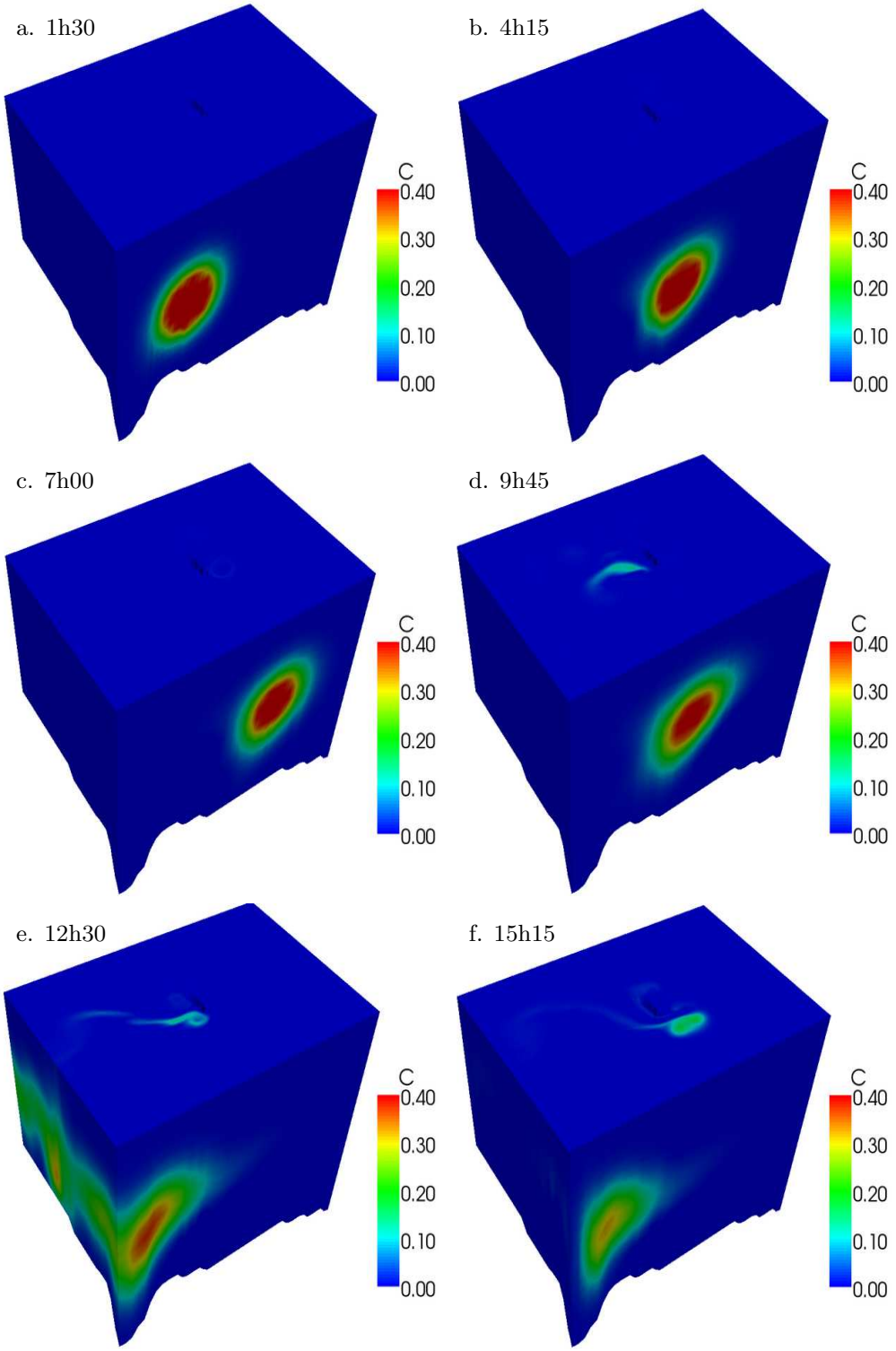

Figure 11: Evolution of a cylindrical tracer patch over a full tidal cycle. (a) Initial condition. (b-c) Falling tide (currents to the right). (d-e) Rising tide (currents to the left). Tide reversals occur around 7h30 and 13h45. The corresponding depth-averaged horizontal velocity field is shown in Figure 7. Vertical tracer diffusion is switched off to focus on vertical advection. Notice the tracer patch at the surface on panels d-f. Velocity from current meter 25 used as open boundary condition.

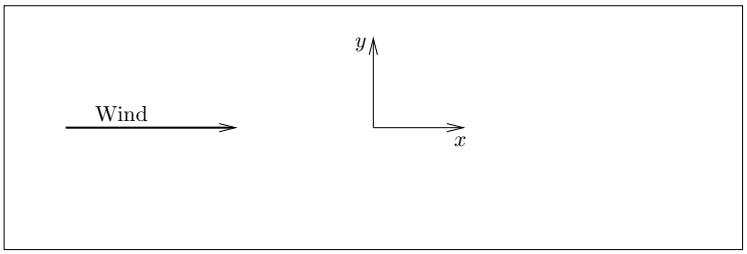

Figure 12: Domain of interest for the wind-driven flow in an elongated basin. Uniform wind is blowing parallel to the x-axis, in the positive direction. All boundaries are closed. The vertical structure of the horizontal flow field is examined across a vertical section at $x = 0$ (see Figure 13).

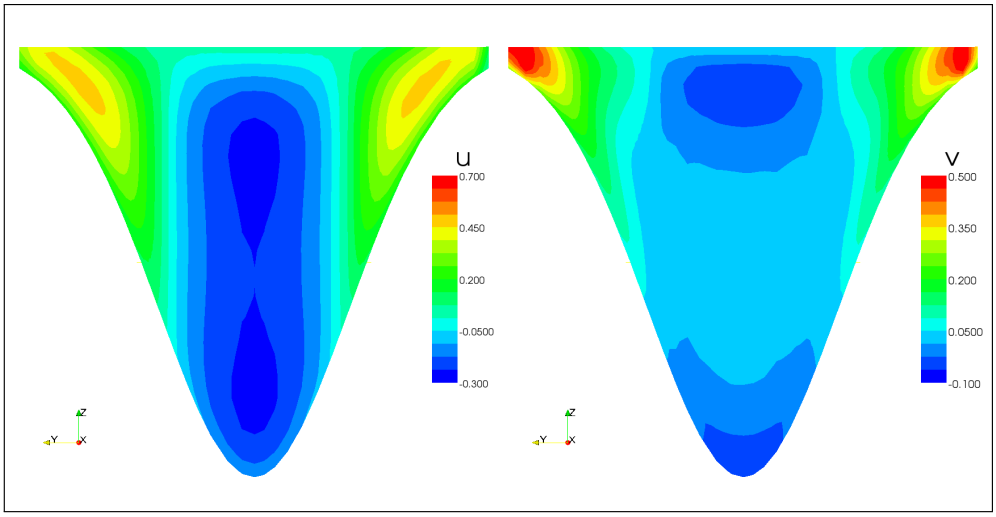

Figure 13: Components of the horizontal velocity field [m s^{-1}] across a vertical section at $x = 0$ (at mid-distance between both ends of the basin). The wind is blowing along the x-axis, in the positive direction. The barotropic transport is upwind (i.e., negative) in the deep part of the basin and downwind (i.e., positive) in the shallow region (see the u-component). However, the surface velocity is everywhere downwind. The vertical structure of the v-component exhibits two co-rotating eddies with negative values near the surface and the bottom and a slow positive returning flow in the interior.